Mechanics of liquid–liquid interfaces and mixing enhancement in microscale flows

STÉPHANE VERGUET[1], CHUANHUA DUAN[1], ALBERT LIAU[2], VEYSEL BERK[3], JAMIE H. D. CATE[4,5,6], ARUN MAJUMDAR[1,7] AND ANDREW J. SZERI[1]†

[1]Department of Mechanical Engineering, University of California, Berkeley, CA 94720, USA

[2]Biophysics Program, University of California, Berkeley, CA 94720, USA

[3]California Institute for Quantitative Biosciences, University of California, Berkeley, CA 94720, USA

[4]Department of Molecular and Cell Biology, University of California, Berkeley, CA 94720, USA

[5]Department of Chemistry, University of California, Berkeley, CA 94720, USA

[6]Physical Biosciences Division, Lawrence Berkeley National Laboratory, CA 94720, USA

[7]Environmental Energy Technologies Division, Lawrence Berkeley National Laboratory, CA 94720, USA

Experimental work on mixing in microfluidic devices has been of growing importance in recent years. Interest in probing reaction kinetics faster than the minute or hour time scale has intensified research in designing microchannel devices that would allow the reactants to be mixed on a time scale faster than that of the reaction. Particular attention has been paid to the design of microchannels in order to enhance the advection phenomena in these devices. Ultimately, *in vitro* studies of biological reactions can now be performed in conditions that reflect their native intracellular environments. Liau *et al.* (*Anal. Chem.*, vol. 77, 2005, p. 7618) have demonstrated a droplet-based microfluidic mixer that induces improved chaotic mixing of crowded solutions in milliseconds due to protrusions ('bumps') on the microchannel walls. Liau *et al.* (2005) have shown it to be possible to mix rapidly plugs of highly concentrated protein solutions such as bovine hemoglobin and bovine serum albumin. The present work concerns an analysis of the underlying mechanisms of shear stress transfer at liquid–liquid interfaces and associated enhanced mixing arising from the protrusions along the channel walls. The role of non-Newtonian rheology and surfactants is also considered within the mixing framework developed by Aref, Ottino and Wiggins in several publications. Specifically, we show that proportional thinning of the carrier fluid lubrication layer at the bumps leads to greater advection velocities within the plugs, which enhances mixing. When the fluid within the plugs is Newtonian, mixing will be enhanced by the bumps if they are sufficiently close to one another. Changing either the rheology of the fluid within the plugs (from Newtonian to non-Newtonian) or modifying the mechanics of the carrier fluid-plug interface (by populating it with insoluble surfactants) alters the mixing enhancement.

1. Introduction

Microchannel mixers that generate chaotic advection (Aref 1984, 2002) have been extensively developed, enabling the mixing of fluids in microscale channels at small

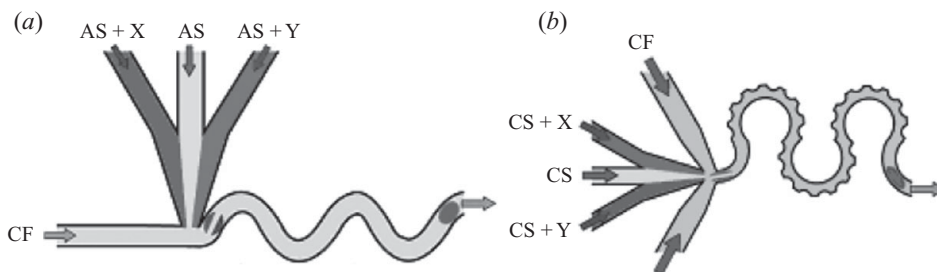† Email address for correspondence: andrew.szeri@berkeley.edu

FIGURE 1. Fast mixing of reactants (top-down view). (*a*) A microfluidic system for the rapid mixing of aqueous solutions (AS). In this micromixer designed by Song *et al.* (2003) and Song & Ismagilov (2003), three separate aqueous streams converge, then intersect with an oil stream as a carrier fluid (CF) and pinch off into droplets (plugs) suspended in the oil carrier fluid. (*b*) Schematic of the bumpy serpentine mixer designed by Liau *et al.* (2005). Two streams of crowded solutions (CS) containing reactants X and Y separated by a third stream of crowded solution intersect with two oil streams (CF) to form long droplets suspended in oil (plugs). The plugs then proceed through several cycles of the bumpy serpentine channel until the plug contents are fully mixed. Note that the plugs encountered experimentally are longer than presented schematically on the figure (see figure 3). (Reprinted with permission from Liau *et al.* 2005. Copyright 2005, American Chemical Society.)

values of the Reynolds number (Liu *et al.* 2000; Stroock *et al.* 2002). In particular, more recently, Song, Tice & Ismagilov (2003), Song & Ismagilov (2003) and Bringer *et al.* (2004) first designed a micromixer for dilute solutions within aqueous droplets suspended in an oil carrier fluid (see figure 1*a*). Three aqueous streams converge in a single microchannel where they pinch off into droplets or 'plugs' in suspension in an oil containing a surfactant. Alternation between two asymmetric counter circulating flow patterns within the plug, as the plug progresses each half-cycle of the serpentine channel (Song *et al.* 2003; Song & Ismagilov 2003; Bringer *et al.* 2004), induces chaotic mixing (Ottino 1989; Ottino & Wiggins 2004; Wiggins & Ottino 2004; Sturman, Ottino & Wiggins 2006). The reaction time coordinate, a measure of the time course of the reaction, is directly related to the distance the plug moves down the channel. The reactants remain confined in each plug, which prevents axial dispersion. Reactions within the plug can thus be submitted to (chemical) kinetic analysis.

The serpentine channel micromixer has been redesigned by Liau *et al.* (2005) who introduced bumps along the outer side of the curved channel walls (see figure 1*b*). With bumps, mixing within long plugs of finite size of highly concentrated proteins (Ellis 2001; Minton 2001; Hall & Minton 2003) was significantly enhanced. The present work concerns an analysis of the means by which the bumps in the experiments of Liau *et al.* (2005) enhance the mixing within the plugs flowing in the microchannel. An additional goal is to explore other means by which one might manipulate the liquid–liquid interfaces in such a system so as to enhance mixing. As we show below, it is the transfer of shear stress across these interfaces that drives the flow within the inner fluid, and hence leads to chaotic advection.

We focus here on elucidating mechanisms, and not on thorough modelling of the flows in every detail. We intend to compare two serpentine mixers of same curvature (see figure 1*b*): one serpentine mixer presents a series of bumps along one wall of the channel, which alternates each half-cycle; the other serpentine mixer is smooth and presents no alteration on its walls. To expose the mechanisms, we shall analyse the arrangement of two infinite fluid layers in a two-dimensional channel, the analysis of which will bring insight to our problem. Consider a microchannel as a
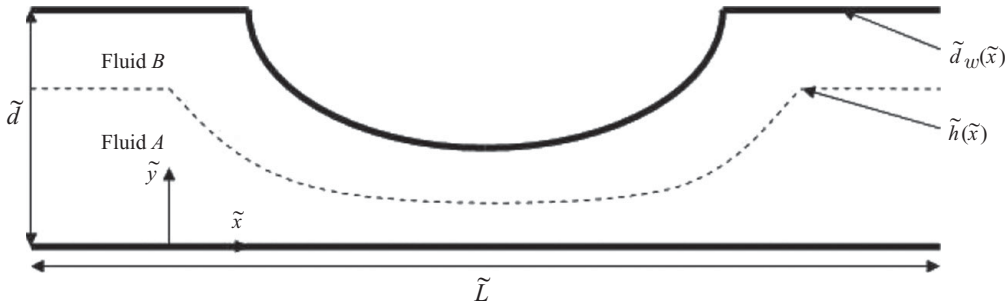
FIGURE 2. Geometry of the model problem (top-down view). The half-width of the channel is represented. The dashed line represents the interface between fluids A and B. The axis $\tilde{x}$ is oriented along the course of the channel. The plane $\tilde{y} = 0$ is interpreted as a plane of symmetry.

two-dimensional halved straight channel which presents a bump in the middle of its course (see figure 2) as a significant unit. The repetition N times of this significant unit will represent one half-cycle with a series of N bumps of the bumpy serpentine mixer designed by Liau *et al.* (2005) (see figure 1*b*). The channel is filled with two immiscible fluids A and B. Both fluids are assumed incompressible and Newtonian, of densities $\tilde{\rho}_A$ and $\tilde{\rho}_B$, of viscosities $\tilde{\mu}_A$ and $\tilde{\mu}_B$. Dimensional quantities are indicated by a tilde. The two-fluid flow is pressure-driven. First, note that our analysis is comparative between smooth and bumpy channels, and that the smooth and the bumpy serpentine micromixers present the same curvature experimentally. Because our comparison with the experiments is focused on the differences between smooth and bumpy channels, we do not explicitly model the effects of channel curvature on the two-layer fluid flow, which has been addressed elsewhere (Roy, Roberts & Simpson 2002; Jensen, Chini & King 2004; Jacob & Gaver 2005; Muradoglu & Stone 2007). The curvature is associated with the reorientation necessary to drive chaotic advection, and because it is the same in smooth and bumpy channels, we focus on the shearing motions that we shall later associate with the twist in the 'linked twist map' (LTM) framework of Sturman *et al.* (2006). Second, note that the droplets experimentally studied span lengths of four times the distance between adjacent bumps (or about 4 bumps) in the bumpy serpentine mixer and exhibit aspect ratios of width with respect to length of 1/4 for the smooth channel to 1/8 for the bumpy channel (see figure 3). In the meantime, the extension of the influence of the front curvature of the droplet on the inner Stokes flow measured relative to the frontal interface of the droplet is limited to less than one half-width of the channel (Behrens *et al.* 1987; Coyle, Blake & Macosko 1987). We shall show that the mixing enhancement due to the presence of the bumps is not sensitive to either (i) the film thickness away from a bump or (ii) the pressure gradient within the long interior of the droplet or the surrounding film. Therefore, we can neglect the influence of pressure gradients due to curvature changes located at the front and at the rear of the droplet and study the case of two infinite fluid layers. One layer (B), that represents the oil lubrication layer, shall be much thinner than the other. In the limit of a long droplet, the model problem as described shares the main features of the physics of a droplet in a serpentine microchannel, with the advantage that the influence of the interfacial mechanics on the flow may be studied with clarity.

Physically, in this paper we demonstrate that the thinning of the lubrication layer B under the bump enhances the shear stress at the interface and that increased shear stress at the interface leads to greater advection velocities in the interior fluid A.

FIGURE 3. Droplets of $50\,\mathrm{mg\,ml}^{-1}$ bovine serum albumine (BSA) visualized with calcein fluorescent dye, along the bumpy serpentine channel, with flow rates of $3\,\mu\mathrm{l\,min}^{-1}$ for the oil stream and $0.3\,\mu\mathrm{l\,min}^{-1}$ for the BSA streams.

This is the basis for the enhancement of mixing. In addition, when the interior fluid is Newtonian, we show that mixing will be enhanced by bumps on the walls of the serpentine channel if the bumps are sufficiently closely spaced to one another. When this is not true, the 'slip difference' (or net shear) between bumpy and smooth channels relaxes to zero. This is the key insight. Also, we show that the slip difference between bumpy and smooth mixers can be made non-zero by changing either the rheology of the interior fluid (from Newtonian to non-Newtonian) or by modifying the mechanics of the interface (by populating it with insoluble surfactants). In that way, the interfacial velocity accelerates less than the centreline velocity under the bump – compared with the Newtonian case – which can result in a positive non-zero slip difference, that persists indefinitely, instead of relaxing to zero.

The plan of the paper is as follows. First, in §2 we present the experimental system, with results (§3) that illustrate the enhancement of mixing by the bumps. Our goal in the analysis that follows is not to develop a computational model of the experiment. Instead, with the experiment as a guide, we develop the simpler flow to study. This has the advantage of possessing all of the key elements of the mixing problem but in a simpler geometry where the exposition of mechanisms is clearer. In §§4–6 we formulate the model problem. In §7, we study how the interfacial transfer of shear stress influences the advection in the interior fluid. This is put into the context of recent work on mixing by Wiggins & Ottino (2004) and Sturman *et al.* (2006). In §8, we explore the way in which the presence of insoluble surfactant on the interface affects the transfer of shear stress (and therefore the mixing enhancement). Appendix B describes the influence of shear thinning and shear thickening. Finally, we give our conclusions.

Taken together, the insight provided by analysis gives valuable guidance in the design of such mixers.

2. Experimental study

2.1. *Fabrication*

The micromixer devices were fabricated with polydimethylsiloxane (PDMS) (Sylgard 184, Dow Corning), using a micromolding process (Duffy *et al.* 1998). To fabricate

the PDMS component, a microchannel mold was made by patterning a silicon wafer with photoresist and etching the silicon approximately $20\,\mu m$ deep in a deep reactive ion etching system (DRIE) system (surface technology systems (STS) advanced silicon etch (ASE) system) to leave a positive relief of channels with a 1:1 aspect ratio. The silicon mold was then placed in a desiccator with a few drops of tridecafluoro-1,1,2,2-tetrahydrooctyl-1-trichlorosilane (United Chemical Technologies) to aid in the future removal of PDMS. PDMS was mixed in a 10:1 ratio of monomer and curing agent, poured over the mold, degassed and cured at $90°C$ for 30 min and then removed from the mold. Inlet and outlet holes were drilled in the PDMS component using a drill (Model 395, Dremel) and $300–400\,\mu m$ diameter drill bits. The molded component was then bonded to a previously prepared PDMS-coated glass slide using a transfer bonding technique (Satyanarayana, Karnik & Majumdar 2005) to obtain the device.

2.2. *Microscopy*

Fluidic connections were made by inserting 0.016 in. outer diameter PTFE tubing (Cole-Parmer) that was connected to 27G needles via 0.012 in. inner diameter PTFE tubing. Glass syringes (Hamilton) were mounted on a syringe pump (SP200I, World Precision Instruments) to control flow through the device. The device was mounted on an inverted epi-fluorescence microscope (TE2000-U, Nikon) for experiments. Images were acquired with an ORCA-ER camera (Hamamatsu Photonics) controlled by Wasabi software (Hamamatsu Photonics). Image analysis was performed with ImageJ and Wasabi.

2.3. *Mixing time scale measurements*

Bovine haemoglobin (Hb) (Sigma) was dissolved in phosphate-buffered saline (Invitrogen). Three solutions, each with same Hb concentration (10, 35 or $100\,mg\,ml^{-1}$), were prepared for each set of Hb mixing time scale measurement experiments: Hb with 1 mM calcium-ion indicator Fluo-4FF (Invitrogen) with 1 mM ethylenediamine tetracetic acid (EDTA) (Sigma), Hb with 1 mM EDTA and Hb with 10 mM $CaCl_2$. Each of these Hb solutions was loaded into one of three $100\,\mu l$ fixed-needle glass syringes (Hamilton). Bovine serum albumin (BSA) mixing time scale measurements were performed with solutions of 10 and $50\,mg\,ml^{-1}$ BSA (Equitech-Bio) in phosphate-buffered saline (Invitrogen). Two of the three $100\,\mu l$ syringes were loaded with BSA and the third syringe was loaded with BSA and 5 mM calcein dye (Invitrogen). In these experiments, a 1:2 v/v mixture of EGC-1702 (3M) and Fluorinert (FC-70, Sigma) with a 1:10 v/v addition of perfluorinated surfactant ($C_6F_{11}C_2H_4OH$, Acros) served as the oil carrier stream and was loaded into two 1 ml removable-needle glass syringes (Hamilton). The three $100\,\mu l$ syringes were driven by syringe pump at flow rates ranging from 0.1 to $0.8\,\mu l\,min^{-1}$ and the 1 ml syringes were driven by an identical syringe pump at flow rates ranging from 0.5 to $4\,\mu l\,min^{-1}$. Ratios between the 1 ml syringes and the $100\,\mu l$ syringes flow rates were kept at 10 to allow the formation of sufficiently long plugs. A third set of experiments was performed with solutions of $35\,mg\,ml^{-1}$ Hb where the oil carrier stream containing a 1:2 v/v mixture of EGC-1702 (3M) and Fluorinert (FC-70, Sigma) had this time different additions (1:10, 1:5 or 1:2 v/v) of perfluorinated surfactant ($C_6F_{11}C_2H_4OH$, Acros).

2.4. *Viscometry and tensiometry*

Viscosities of Hb and BSA solutions were derived from prior studies (Andreas, Hauser & Tucker 1938; Monkos 1994, 1996). The Fluorinert, EGC-1702, surfactant mixture (oil carrier fluid) was measured by Liau *et al.* (2005) using a falling ball viscometer (Gilmont). Interfacial tensions of oil carrier fluid and the Hb and BSA

Hb solution concentration	Viscosity (mPa s)
10 mg ml^{-1}	1.05
35 mg ml^{-1}	1.17
100 mg ml^{-1}	1.63
BSA solution concentration	
10 mg ml^{-1}	1.00
50 mg ml^{-1}	1.00
Oil stream	
1:10 surfactant	4.88 $\pm$ 0.06
Experimental combinations	Interfacial tension (mN m^{-1})
10 mg ml^{-1} Hb – 1:10 surfactant	3.61 $\pm$ 0.97
35 mg ml^{-1} Hb – 1:10 surfactant	3.47 $\pm$ 0.47
100 mg ml^{-1} Hb – 1:10 surfactant	2.90 $\pm$ 0.23
10 mg ml^{-1} BSA – 1:10 surfactant	5.99 $\pm$ 0.59
50 mg ml^{-1} BSA – 1:10 surfactant	5.94 $\pm$ 0.44

TABLE 1. Calculated values of the viscosity and interfacial tension measurements for the different samples used in the experiments.

Hb concentration	10 mg ml^{-1}	35 mg ml^{-1}	100 mg ml^{-1}
Λ	0.22	0.24	0.33
Number of half-cycles for full mixing in smooth channel (experimental)	6	7	12
Number of half-cycles M for full mixing in bumpy channel (experimental)	3	4	7

TABLE 2. Experimental results obtained for samples of different Hb concentrations with flow rates of 2 μl min^{-1} for the oil stream and 0.2 μl min^{-1} for Hb streams. $\Lambda = \tilde{\mu}_A / \tilde{\mu}_B$ is a dimensionless viscosity ratio between the inner fluid A within the plug and the oil outer fluid B and is later introduced in §5.

solutions were measured by an inverted pendant drop technique. Pendant drop images were captured using a drop shape analysis system (Kruss, DSA-10). Interfacial tensions were extracted using the method of a selected plane and tables listed by Andreas *et al.* (1938) and Stauffer (1965). Table 1 collects the results.

3. Results

Mixing of Hb samples of different concentrations in plugs carried by an oil stream containing a 1:10 v/v addition of perfluorinated surfactant ($C_6F_{11}C_2H_4OH$, Acros) in both smooth and bumpy mixers has been analysed for flow rates of 0.2 μl min^{-1} and 2 μl min^{-1} for respectively the Hb streams and the oil stream (see table 2). We plotted on figure 4 experimental data concerning the mixing of 35 mg ml^{-1} Hb solutions.

Mixing becomes more difficult even in bumpy channels for higher Hb concentrations (see 100 mg ml^{-1} concentration). As the concentration rises, the crowding effect of hemoglobin on mixing becomes more and more important. Specifically, we expect that hemoglobin adsorbs more at the interface when its concentration increases. The data in table 1 would appear to confirm this suspicion as it shows the interfacial tension diminishes when the concentration of the Hb sample is increased. It seems that the advection velocities in the experiment are increased, perhaps because the
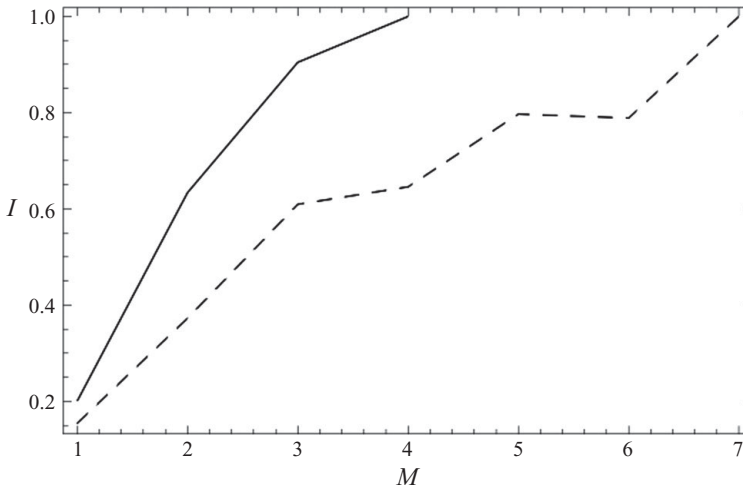
FIGURE 4. Mixing of $35\,\mathrm{mg\,ml^{-1}}$ Hb in smooth and bumpy mixers. Fluorescence intensity I, proportional to the concentration of the species produced by the binding of calcium ions to the fluorescent dye, as a function of the number of half-cycles M passed through the serpentine mixer. Dashed line: smooth mixer with flow rates of 0.2 and $2\,\mu\mathrm{l\,min^{-1}}$ for respectively the Hb streams and the oil stream. Solid line: bumpy mixer with flow rates of 0.2 and $2\,\mu\mathrm{l\,min^{-1}}$ for respectively the Hb streams and the oil stream.

interface is heavily crowded with Hb adsorbed and shear moves the interface in a more solid-like fashion owing to the close-packed Hb. The role of interfacial effects is addressed later on in this paper.

4. Formulation

For analysis we shall consider the top half of a channel with symmetrically placed bumps on both sides (see figure 2). Fluid A represents the outer oil carrier fluid whereas fluid B represents the inner fluids to be mixed. The lower half of the channel can be obtained using a symmetry with respect to the centreline of the channel. The plane $\tilde{y}=0$ is not a plane of symmetry in the experimental channel (figure 1). However, we have also pursued calculations in the non-symmetric channel (bump on one side only) and found similar results in all significant respects as presented in the following sections: slip difference relaxing to zero after passage under a bump, enhancement of interfacial stress at a bump, independence of the enhancement on the lubrication layer thickness $h(0)$. These facts are qualitatively exactly the same as in the case of the symmetric channel, but with decreased quantitative magnitudes. Therefore, we shall study the symmetric case for ease of exposition.

In the experiments, the plugs in the bumpy channels span about four times the distance $\tilde{L}$ between adjacent bumps, which corresponds to a dimensionless length of 4. In the literature (Behrens *et al.* 1987; Coyle *et al.* 1987) there are estimates of the disturbance to the flow associated with the front and the rear of the plugs; these occur over dimensionless lengths of $1/2 \times 1/8 \times 4 = 1/4$. Recall that the width to length ratio of the plugs in bumpy channels is about 1/8 experimentally and that the front and rear perturbations extend each of about 1/2 of the dimensionless width of the plug. As $1/4 + 1/4 = 1/2 \ll 4$, it is reasonable to neglect recirculation patterns. In other words, we do not take into account the pressure gradients localized at the front and rear of the plugs.

When a finite drop interacts with the next bump, we expect a slight modulation of the speed of the drop occurs. This would involve a deceleration before the bump, followed by acceleration afterwards. This modulation in speed as a next bump is encountered by the leading edge would also be associated with a time-dependent modulation of the pressure gradient. This becomes unsteady. The bump represents an obstacle to the drop passage requiring bending of the interface and thinning of the lubrication layer. However, the temporal modulation in $\mathrm{d}p/\mathrm{d}x$, associated with the finiteness of the drop simply does not matter in our qualitative explanation of mixing enhancement, it is factored out in our analysis (see (7.1)). Therefore, we can neglect the influence of long-range pressure gradients induced by the leading edge of the droplet encountering the next bump. We study therefore the case of two infinite fluid layers. In this case, the mass conservation of the long drop volume is attained as the mass flux per length across the width of the internal fluid A remains constant far from the drop's leading edge (see §6).

The geometry of the wall is prescribed by the channel half-width $\tilde{d}_w(\tilde{x})$. The interface between the two fluids is located at $\tilde{y} = \tilde{h}(\tilde{x})$. This material line can be oriented by the normal $\boldsymbol{e}_n$ and tangent $\boldsymbol{e}_t$ vectors at the interface. The interfacial curvature is given by $\tilde{\kappa} = -\tilde{\nabla}_S \cdot \boldsymbol{e}_n$ where $\tilde{\nabla}_S = [\boldsymbol{I} - \boldsymbol{e}_n \otimes \boldsymbol{e}_n] \cdot \tilde{\nabla}$ is the surface gradient operator (Deen 1998). Hence, $\tilde{\kappa} = (\mathrm{d}^2\tilde{h}/\mathrm{d}\tilde{x}^2)[1 + (\mathrm{d}\tilde{h}/\mathrm{d}\tilde{x})^2]^{-3/2}$. Neglect of second-order terms in $\mathrm{d}\tilde{h}/\mathrm{d}\tilde{x}$ leads to the simpler forms $\tilde{\kappa} \sim \mathrm{d}^2\tilde{h}/\mathrm{d}\tilde{x}^2$, $\boldsymbol{e}_n \sim (-\mathrm{d}\tilde{h}/\mathrm{d}\tilde{x})\boldsymbol{e}_{\tilde{x}} + \boldsymbol{e}_{\tilde{y}}$, $\boldsymbol{e}_t \sim \boldsymbol{e}_{\tilde{x}} + (\mathrm{d}\tilde{h}/\mathrm{d}\tilde{x})\boldsymbol{e}_{\tilde{y}}$, $\tilde{\nabla}_S = \boldsymbol{e}_{\tilde{x}}(\partial/\partial\tilde{x}) + \boldsymbol{e}_{\tilde{y}}(\mathrm{d}\tilde{h}/\mathrm{d}\tilde{x})(\partial/\partial\tilde{y})$. The steady state assumption also leads to $\partial/\partial\tilde{t} = 0$.

4.1. *Navier–Stokes equations*

The balance of linear momentum for both fluids A and B reads

$$\tilde{\rho}_A \tilde{\boldsymbol{u}}_A \cdot \tilde{\nabla} \tilde{\boldsymbol{u}}_A = -\tilde{\nabla} \tilde{p}_A + \tilde{\mu}_A \tilde{\nabla}^2 \tilde{\boldsymbol{u}}_A, \tag{4.1}$$

$$\tilde{\rho}_B \tilde{\boldsymbol{u}}_B \cdot \tilde{\nabla} \tilde{\boldsymbol{u}}_B = -\tilde{\nabla} \tilde{p}_B + \tilde{\mu}_B \tilde{\nabla}^2 \tilde{\boldsymbol{u}}_B. \tag{4.2}$$

The incompressibility of the fluids leads to

$$\frac{\partial \tilde{u}_i}{\partial \tilde{x}} + \frac{\partial \tilde{v}_i}{\partial \tilde{y}} = 0, \quad i = A, B. \tag{4.3}$$

4.2. *Boundary conditions*

For the horizontal velocities we have: no slip at the wall, $\tilde{u}_B(\tilde{x}, \tilde{d}_w(\tilde{x})) = 0$; symmetry condition at $\tilde{y} = 0$, $(\partial \tilde{u}_A/\partial \tilde{y})(\tilde{x}, 0) = 0$; continuity of the horizontal velocity field at the interface, $\tilde{u}_A(\tilde{x}, \tilde{h}(\tilde{x})) = \tilde{u}_B(\tilde{x}, \tilde{h}(\tilde{x}))$. For the vertical velocities we have: no penetration at the wall, $\tilde{v}_B(\tilde{x}, \tilde{d}_w(\tilde{x})) = 0$; no penetration at $\tilde{y} = 0$, $\tilde{v}_B(\tilde{x}, 0) = 0$; continuity of the vertical velocity at the interface, $\tilde{v}_A(\tilde{x}, \tilde{h}(\tilde{x})) = \tilde{v}_B(\tilde{x}, \tilde{h}(\tilde{x})) = \tilde{u}_A(\tilde{x}, \tilde{h}(\tilde{x}))(\mathrm{d}\tilde{h}/\mathrm{d}\tilde{x})$ (where continuity of the horizontal velocity at the interface and steadiness have been implicitly used).

4.3. *Normal and tangential stress balances at the interface*

The Young–Laplace equation at the interface A–B is given by

$$[\boldsymbol{e}_n \cdot \tilde{\boldsymbol{T}}_i \; \boldsymbol{e}_n]_{A-B} = \tilde{\gamma}\tilde{\kappa}, \tag{4.4}$$

where $\tilde{\gamma}$ is the surface tension at the interface (one-dimensional $\tilde{\gamma}(\tilde{x})$), $\tilde{\kappa}$ is the curvature and $\tilde{\boldsymbol{T}}_i$ is the Cauchy stress tensor of the fluid i. Neglect of second-order

terms in $\mathrm{d}\tilde{h}/\mathrm{d}\tilde{x}$ and (4.4) leads to

$$\tilde{p}_A - \tilde{p}_B + 2\tilde{\mu}_B \frac{\partial \tilde{v}_B}{\partial \tilde{y}}(\tilde{x}, \tilde{h}(\tilde{x})) - 2\tilde{\mu}_A \frac{\partial \tilde{v}_A}{\partial \tilde{y}}(\tilde{x}, \tilde{h}(\tilde{x})) = \tilde{\gamma}\frac{\mathrm{d}^2\tilde{h}}{\mathrm{d}\tilde{x}^2}. \tag{4.5}$$

The tangential stress balance at the interface A–B is computed from

$$[e_t \cdot \tilde{T}_i\, e_n]_{A-B} = -e_n \cdot \tilde{\nabla}_S \tilde{\gamma}. \tag{4.6}$$

Further manipulation leads to the following expression:

$$\tilde{\mu}_B \frac{\partial \tilde{u}_B}{\partial \tilde{y}}(\tilde{x}, \tilde{h}(\tilde{x})) - \tilde{\mu}_A \frac{\partial \tilde{u}_A}{\partial \tilde{y}}(\tilde{x}, \tilde{h}(\tilde{x})) = -\frac{\mathrm{d}\tilde{\gamma}}{\mathrm{d}\tilde{x}}. \tag{4.7}$$

5. Dimensionless variables

Now we introduce the dimensionless variables through $\tilde{x} = \tilde{L}x$, $\tilde{y} = \tilde{d}y$, $\tilde{h} = \tilde{d}h$, $\tilde{d}_w = \tilde{d}d_w$, $\tilde{u}_i = \tilde{U}u_i$, $i = A, B$. $\tilde{L}$ and $\tilde{d}$ refer to the lengths given on figure 2. Elsewhere in the following, x and y are then dimensionless *with different scales*. $\tilde{U}$ is a scaling for the horizontal velocity field. It shall be related to an experimental flow rate $\tilde{Q}$. Define the lubrication parameter $\epsilon = \tilde{d}/\tilde{L}$ and look for a scaling of the vertical velocity field $\tilde{V}$ and of the pressures $\tilde{p}_A$ and $\tilde{p}_B$. The mass conservation equation immediately gives $\tilde{V} = \epsilon\tilde{U}$.

We define a Reynolds number $Re = \tilde{\rho}_B \tilde{U}\tilde{d}/\tilde{\mu}_B$. A scaling for the pressures is chosen as $\tilde{P}_A = \tilde{P}_B = (\tilde{\mu}_B\tilde{U})/(\tilde{d}\epsilon) = (\tilde{\mu}_B\tilde{U}\tilde{L})/\tilde{d}^2$. We take the limit $(\epsilon Re, \epsilon) \rightarrow (0, 0)$. The lubrication approximation leads to

$$\frac{\partial p_A}{\partial x} = \Lambda\frac{\partial^2 u_A}{\partial y^2}, \tag{5.1}$$

$$\frac{\partial p_A}{\partial y} = 0, \tag{5.2}$$

$$\frac{\partial p_B}{\partial x} = \frac{\partial^2 u_B}{\partial y^2}, \tag{5.3}$$

$$\frac{\partial p_B}{\partial y} = 0. \tag{5.4}$$

A viscosity ratio $\Lambda = \tilde{\mu}_A/\tilde{\mu}_B$ emerges as a relevant parameter. Dimensionless continuity equations read

$$\frac{\partial u_i}{\partial x} + \frac{\partial v_i}{\partial y} = 0, i = A, B, \tag{5.5}$$

The dimensionless boundary conditions read

$$u_B(x, d_w(x)) = 0, \quad u_A(x, h(x)) = u_B(x, h(x)), \quad \frac{\partial u_A}{\partial y}(x, 0) = 0, \tag{5.6}$$

$$v_B(x, d_w(x)) = 0, \quad v_A(x, 0) = 0, \quad v_A(x, h(x)) = v_B(x, h(x)) = u_A(x, h(x))\frac{\mathrm{d}h}{\mathrm{d}x}. \tag{5.7}$$

Dimensionless Young–Laplace equation and tangential stress balance are as follows: in dimensionless variables (4.5) reads

$$p_A - p_B - 2\epsilon^2\left[\Lambda\frac{\partial v_A}{\partial y}(x, h(x)) - \frac{\partial v_B}{\partial y}(x, h(x))\right] = \frac{\epsilon^3}{Ca}\gamma\frac{\mathrm{d}^2 h}{\mathrm{d}x^2}. \tag{5.8}$$

We define the capillary number $Ca = (\tilde{\mu}_B \tilde{U})/\tilde{\gamma}_0$ where the A–B interfacial surface tension $\tilde{\gamma}(\tilde{x}) = \tilde{\gamma}_0 \gamma(x)$ has the scaling $\tilde{\gamma}_0$, which shall be related to experimental surface tensions. In the same way, (4.7) becomes

$$\frac{\partial u_B}{\partial y}(x, h(x)) - \Lambda \frac{\partial u_A}{\partial y}(x, h(x)) = -\frac{\epsilon}{Ca} \frac{\mathrm{d}\gamma}{\mathrm{d}x}. \tag{5.9}$$

Three distinct cases are to be explored. Case I. $\epsilon \ll Ca$, where the surface tension plays a subdominant role. We then have $p_A = p_B = p$ and

$$\frac{\partial u_B}{\partial y}(x, h(x)) = \Lambda \frac{\partial u_A}{\partial y}(x, h(x)). \tag{5.10}$$

It is the case for instance where $Ca \to \infty$; in other words where there is no surface tension at the interface A–B. Equation (5.10) can also be obtained when the interfacial tension is uniform. Case II. $\epsilon \sim Ca$, which corresponds to the experimental case (see §8), where the surface tension affects both balances. Neglect of second and higher orders in ϵ and the normal stress balance becomes $p_A = p_B = p$. Also, the tangential stress balance is obtained as the following:

$$\frac{\partial u_B}{\partial y}(x, h(x)) - \Lambda \frac{\partial u_A}{\partial y}(x, h(x)) \sim -\frac{\mathrm{d}\gamma}{\mathrm{d}x}. \tag{5.11}$$

Case III. $\epsilon \gg Ca$, where the scaling used thus far becomes inconsistent. This case, which corresponds to some microfluidic applications, remains for future work. A starting point would be to formulate a perturbation expansion with a uniform surfactant concentration making rigid the interface at the leading order and a small perturbation balancing the viscous shear stresses in magnitude (Park 1992).

6. Uniform interfacial surface tension

We now assume the interface between the two fluids possesses a surface tension and that this surface tension is uniform (i.e. Case I). In this case, the tangential stress balance is given by (5.10). The situation is physically equivalent to the case $\epsilon \ll Ca$, with no tension at the interface. The dimensionless horizontal velocity fields are easily computed:

$$u_A(x, y) = \frac{1}{2\Lambda} \frac{\mathrm{d}p}{\mathrm{d}x}[y^2 - h^2(x)] + \frac{1}{2} \frac{\mathrm{d}p}{\mathrm{d}x}[h^2(x) - d_w^2(x)], \tag{6.1}$$

$$0 \leqslant x \leqslant 1, \quad 0 \leqslant y \leqslant h(x),$$

$$u_B(x, y) = \frac{1}{2} \frac{\mathrm{d}p}{\mathrm{d}x}[y^2 - d_w^2(x)], \tag{6.2}$$

$$0 \leqslant x \leqslant 1, \quad h(x) \leqslant y \leqslant d_w(x).$$

We note that both fluid velocities are linearly proportional to the same pressure gradient, whether it is steady or unsteady. The continuity equation (5.5) and corresponding boundary conditions (5.6), (5.7) remain unchanged. The shear stress at the interface A–B is then given by

$$\tau_{AB}(x) = \frac{\partial u_B}{\partial y}(x, h(x)) = -\Lambda \frac{\partial u_A}{\partial y} = -p'(x)h(x), \tag{6.3}$$

where (6.2) has been used. We assume $d_w(0) = 1$. Analytical solutions are obtained by solving the Reynolds lubrication equations for fluids A and B derived from the continuity equations (5.5) and corresponding boundary conditions (5.6) and (5.7). The
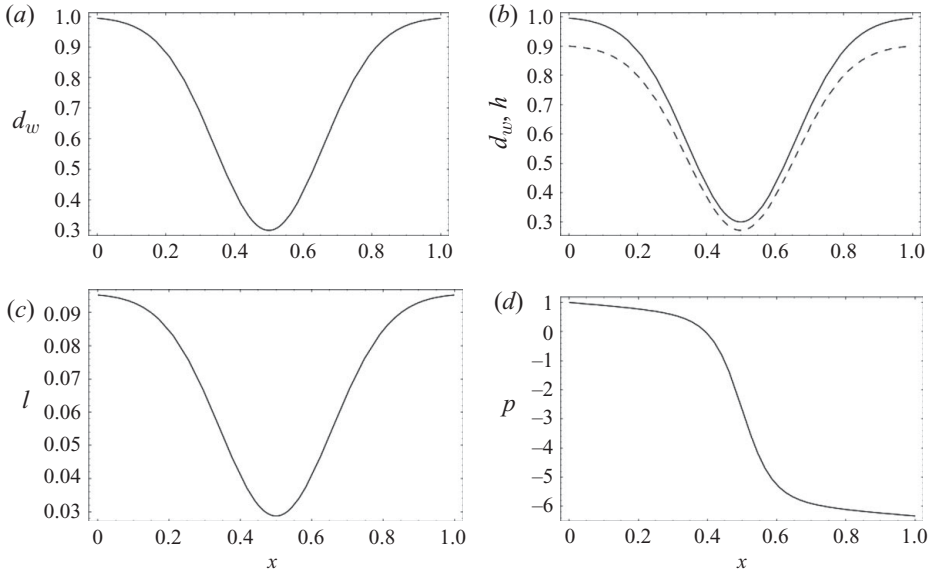
FIGURE 5. (*a*) Prescribed wall profile $d_w(x)$ of the channel. (*b*) Interface $h(x)$ (dashed) and wall $d_w(x)$ profiles. (*c*) Lubrication layer thickness $l(x) = d_w(x) - h(x)$. (*d*) Pressure profile $p(x)$ in the channel. All quantities are dimensionless.

dimensionless relevant results hereby follow:

$$h(x) = h(0)d_w(x), \tag{6.4}$$

$$p'(x) = -\frac{1}{d_w^3(x)}, \tag{6.5}$$

$$\tau_{AB}(x) = \frac{h(0)}{d_w^2(x)}. \tag{6.6}$$

The dimensionless thickness of the lubrication layer is given by $l(x) = (1 - h(0))d_w(x)$. Therefore, τ_{AB} has a maximum at the apex of the bump. This location corresponds to a minimum for the thickness of the lubrication layer and also to an inflexion point for the pressure profile (see figures 5*c* and 5*d*) as shown analytically with the expression $p''(x) = 3d'_w(x)/d_w^4(x)$ (see figure 5*b*).

Next, we use (6.4) and (6.5) and replace in (6.1) and (6.2) to find the following expressions for the horizontal velocity fields:

$$u_A(x, y) = \frac{1}{2\Lambda d_w(x)}\left[(1 - h(0)^2)\Lambda + h^2(0) - \frac{y^2}{d_w^2(x)}\right], \quad 0 \leqslant x \leqslant 1, 0 \leqslant y \leqslant h(x), \tag{6.7}$$

$$u_B(x, y) = \frac{1}{2d_w(x)^3}\left[d_w^2(x) - y^2\right], \quad h(x) \leqslant y \leqslant d_w(x). \tag{6.8}$$

In the same way, the horizontal velocity fields at the interface and at $y = h(x)$ and $y = 0$ are

$$u_h(x) = u_B(x, h(x)) = \frac{[1 - h^2(0)]}{2d_w(x)}, \tag{6.9}$$

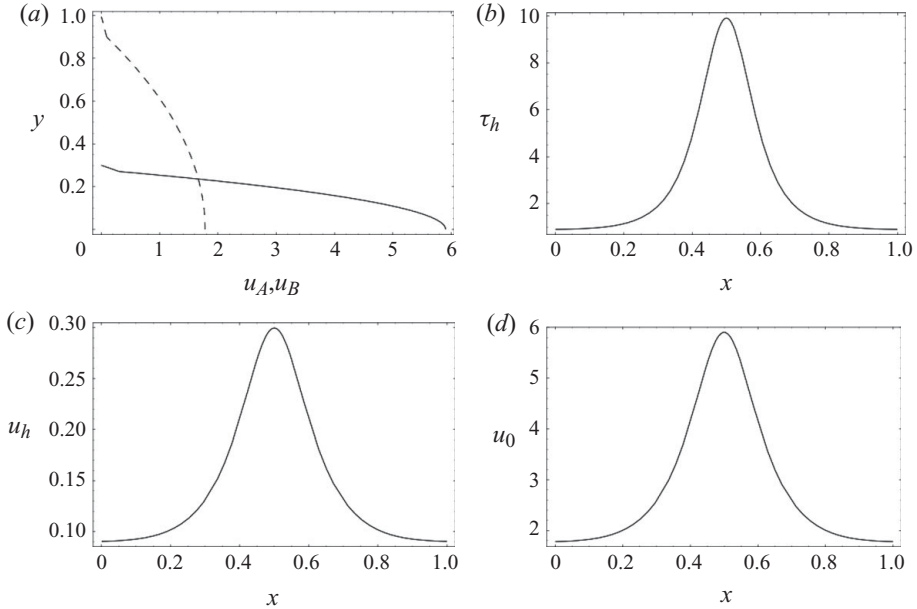$$u_0(x) = u_A(x, 0) = \frac{[1 - h^2(0)]}{2d_w(x)} + \frac{h^2(0)}{2\Lambda d_w(x)}. \tag{6.10}$$

FIGURE 6. (a) Horizontal velocity profiles far from (dashed) and under the bump. (b) Shear stress at the interface $y = h(x)$ between the two fluids along the channel. (c) Horizontal velocity u_h at the interface $y = h(x)$ along the channel. (d) Horizontal velocity u_0 in the middle of the channel at $y = 0$ along the channel. All quantities are dimensionless.

We look at the solution $\{p(x), h(x)\}$ for a wall profile (bump) prescribed as a Gaussian function $d_w(x) = 1 - a e^{-b(x-1/2)^2}$ (see figure 5a) (see Appendix A for details). The analytical solutions for interface profile (6.4), thickness of the lubrication layer and pressure (6.5) are plotted thereafter (see figures 5b, 5c and 5d) where $h(0) = 0.90$, $\Lambda = 0.24$, $a = 0.7$, $b = 20$. The choice of parameters is intended to be suggestive of the experimental conditions. $h(0)$ was determined in accordance with interfacial surface tension measurements (see table 1; Bretherton 1961) and verified visually.

At the bump at $x = 1/2$, there is an inflexion point for the pressure profile and a thinning of the lubrication layer. A minimum in the wall profile under the bump leads also to a maximum in the shear stress (6.6). At the same time, it provides a maximum for the horizontal velocities at the interface $y = h(x)$ (6.9) and at $y = 0$ (6.10). These results can be seen in figure 6. Physically, the thinning of the lubrication layer B under the bump enhances the shear stress at the interface. Increased shear stress at the interface leads to greater advection velocities in the interior fluid. This is the basis for the enhancement of mixing.

Quantitatively, we find that the interfacial shear stress under the bump is enhanced by about 11 times as compared to far from the bump. The thickness of the film upstream of the bump $h(0)$ is controlled by the mechanics near the drop's leading edge (Bretherton 1961; Hodges, Jensen & Rallison 2004). However, considering the expression for the interfacial shear stress (6.6), we observe that the ratios of these quantities between the cases with bump and without bump are independent of $h(0)$. Owing to this independence of $h(0)$, the enhancement of convection through the introduction of bumps is independent of $h(0)$, thus independent of Ca. The magnitude of the external film thickness $h(0)$ has only a quantitative effect on mechanisms of
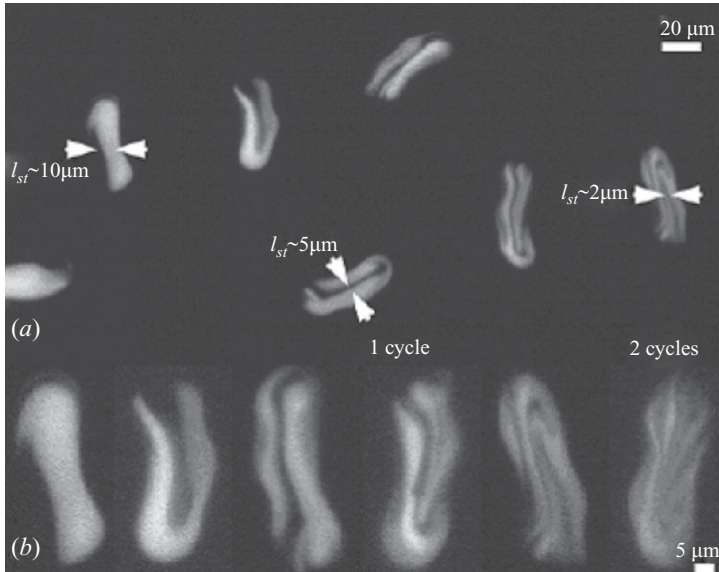
FIGURE 7. Mixing of plugs composed of two-thirds $300\,\mathrm{mg\,ml}^{-1}$ Hb and one-third $260\,\mathrm{mg\,ml}^{-1}$ BSA characterized by examination of striations as visualized with calcein fluorescent dye. A high concentration of calcein dye (5 mM) is initially confined to the one-third of the plug (BSA part) but is rapidly redistributed by folding of the plug contents. (*a*) Striation thickness along the bumpy serpentine mixer. (*b*) Images of plugs after every half-cycle along the bumpy serpentine channel reveal striations folding in greater detail. Note that the pictures are taken from the cross-section view (see figures 1 and 2). (Reprinted with permission from Liau *et al.* (2005). Copyright 2005, American Chemical Society.)

mixing. We observe then stronger convective motions in the fluid phase not in contact in the wall, which corresponds to stronger convective motions within the long plugs.

7. Quantification of the influence of bumps on mixing

We now want to relate the previous analysis to the mixing problem experimentally conducted by Liau *et al.* (2005). At this point, we interpret the main elements of the mixing problem in the framework of the LTM introduced by Wiggins & Ottino (2004) and Sturman *et al.* (2006). The LTM framework mathematically captures the paradigm of 'crossing of streamlines', sufficient condition for chaotic mixing. Indeed, the flow along the course of the serpentine channel is 'segmented' due to a time periodic change in the channel geometry: the alternation of two subunits as the location of the bumps alternates from one side of the wall to the other side of the wall. In each subunit, there is a distinct flow pattern with a specific 'twist', namely a specific shear gradient across streamlines. Two distinct flow patterns are then superimposed, which enables 'crossing of streamlines'. The succession of two subunits (or half-cycles) constitute a cycle, and the flow can be described by a mapping from the beginning of the cycle to the end of the cycle. The latter mapping is the composition of two mappings, each a twist map. The first twist map is the mapping of particles in the cross-section at the beginning of the cycle to the cross-section at the half-cycle. The second twist map is the mapping of particles from the cross-section at the end of the half-cycle to the cross-section end of the cycle. The cross-section retained is sketched on figure 2. Indeed, striations along these two dimensions are observed experimentally in the plugs (see figure 7).
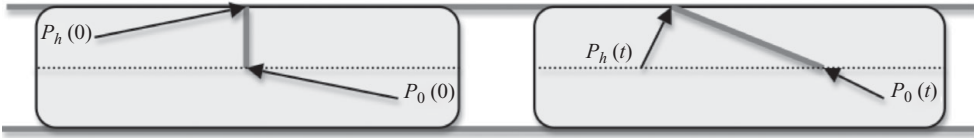
FIGURE 8. Sketch of the evolution of the slip with time t in the case of a plug flowing in a straight channel. The solid lines link particles P_0 and P_h. Recall that in the experimental reality, the plugs are very long and present long rectangular shapes (see figure 3).

Hence, in the simplest framework, the flow may be seen as an elongational flow. It is a succession of simple shear flows with periodic reorientation of material elements relative to the flow streamlines, which can be further simplified to a sequence of constant alternating shears (D'Alessandro, Dahleh & Mezic 1999). The shear or 'twist' will occur during the passage under a series of bumps during one half-cycle. Then, the reorientation will occur when the plug transitions from one half-cycle to the next half-cycle. Then a new shear or new 'twist' will occur during the passage under a new series of bumps during the next half-cycle... etc. Now, keeping in mind our goal to examine the differences between the flow in the serpentine channel with and without bumps, it is clear that we should focus on the shearing flow that provides the twist. After all, the re-orientation step is the same in the channels with and without bumps. In our approach, we slightly differ from Ottino & Wiggins (2004) and Sturman *et al.* (2006), however. Indeed, we are not looking at a uniform shear rate but rather at a net shear, which captures better the transient influence of the passage past a bump.

Stirring occurs by producing the maximum amount of interfacial area between two initially segregated fluids and mixing occurs once the effects of diffusion are included (Aref 2002). In two dimensions, the creation of interfacial area is connected to the stretching of lines. The strength of the stretching is accounted by the net shear. In a compact domain, mixing can be quantified by the striation thickness (see figure 7), which shows that the flow within the plugs can be interpreted two dimensionally. The striation thickness is inversely proportional to the interfacial area, due to the incompressibility of the flow.

In the present work, we shall estimate the stretching that occurs as the two fluids go past the bump. For this purpose, we interpret the flow as a transient shear flow between a fluid particle P_0 located at the centreline of the channel and a fluid particle P_h located at the interface between the two fluids. The stretching, or more precisely the striation thickness, will be determined from the estimated net shear associated with the passage of a series of N bumps. The net shear is evaluated through a slip analysis described in the following section. We determine then the striation thickness after N bumps as a function $s(N)$. The bumps are responsible for the development of twist; hence the flow fits nicely into the useful framework of LTM introduced by Wiggins & Ottino (2004) and Sturman *et al.* (2006), with the subtle difference we look here at a net shear and not at a shear rate. Moreover, we can estimate the contribution of the bumps to stretching in the flow using our simplified channel flow geometry.

7.1. *Interpretation in terms of slip*

We compute the 'slip' (or relative longitudinal displacement) between a particle of fluid P_0 located in the middle of the channel at $y = 0$ and a particle of fluid P_h located at the interface $y = h(x)$ (see figure 8). That slip will correspond to the net

shear described in the previous paragraph. In fact, we look at the evolution of the segment $[P_0 P_h]$, more precisely at the difference in horizontal coordinates of these two particles (slip) at a time t: $x_s(t) = x_0(t) - x_h(t)$. We then compare that relative longitudinal displacement, which we name here the difference of slip $\Delta x_s(t)$ between the case of a plug flowing in a straight channel and the case of a plug flowing in a channel having a bump on its upper wall (see figure 2).

The particles' horizontal coordinates in the centreline of the channel and at the interface can be described as the following functions $x_0(t) = x_0(t, x_0(0))$ and $x_h(t) = x_h(t, x_h(0))$. We assume that the particles start from the vertical axis of symmetry of the plugs so that $x_h(0) = x_0(0) = 0$. We look at the particle paths for P_0 and P_h as the following $dx_0/dt = u_0(x_0)$ and $dx_h/dt = u_h(x_h)$. We eliminate time t and link x_h with x_0 to obtain a relationship $x_h(x_0)$. In other words,

$$\frac{dx_h}{dx_0} = C \frac{d_w(x_0)}{d_w(x_h)}, \tag{7.1}$$

where $C = (1 + h^2(0)\Lambda^{-1}(1 - h^2(0))^{-1})^{-1}$ and we have used (6.9) and (6.10). We define the slip as a function of x_0: $x_s(x_0) = x_0 - x_h(x_0)$; the latter relationship will be computed in the cases of bumpy and smooth channels, in order to assess the effect of the bumps. Note that because u_0 and u_h are both linear in dp/dx (see (6.9) and (6.10)), the temporal modulation in dp/dx associated with the finiteness of the drop (mentioned in §4) is irrelevant to our explanation of mixing enhancement as the temporal modulation of dp/dx factors out in (7.1).

7.1.1. *Smooth channel*

As the channel is straight, we have the straightforward relation between the particles' horizontal positions from (7.1):

$$\frac{dx_h}{dx_0} = C. \tag{7.2}$$

Hence the slip in the case of no bumps is $x_{s_{nb}} = (1 - C)x_0$. Recall that $x_0(t) = (1 - h^2(0)(1 - \Lambda^{-1}))t/2$; we find eventually:

$$x_{s_{nb}} = \frac{h^2(0)}{2\Lambda}t. \tag{7.3}$$

7.1.2. *Bumpy channel*

The relation between the particles' horizontal positions changes with the introduction of a bump in the channel. In other words,

$$dx_h d_w(x_h) = \frac{1 - h^2(0)}{2} dt, \tag{7.4}$$

where dx_h represents the differential change of the dimensionless coordinate x_h during the differential dimensionless time dt. We write $d_w(x) = 1 - f(x)$ (where $f(x)$ is the bump shape) and use implicitly $x_h(0) = 0$ to integrate between $t = 0$ and t:

$$x_{h_b}(t) - \int_0^{x_{h_b}(t)} f(x)\, dx = \frac{1 - h^2(0)}{2}t. \tag{7.5}$$

Similarly, we find

$$x_{0_b}(t) - \int_0^{x_{0_b}(t)} f(x)\, dx = \frac{1 - h^2(0)}{2}t + \frac{h^2(0)}{2\Lambda}t. \tag{7.6}$$
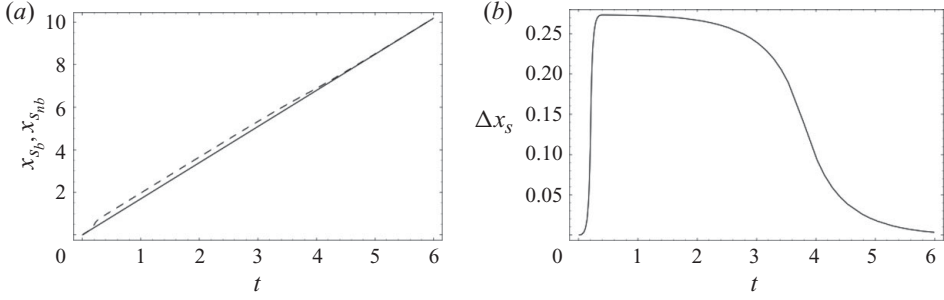
FIGURE 9. Slips and slip difference as a function of time t for $h(0) = 0.90$, $\Lambda = 0.24$, $a = 0.7$ and $b = 20$. (a) Slips $x_{s_b}(t)$ for the bumpy channel (dashed) and $x_{s_{nb}}(t)$ for the smooth channel. (b) Evolution of the slip difference $\Delta x_s(t) = x_{s_b}(t) - x_{s_{nb}}(t)$ between bumpy and smooth channels with dimensionless time t. All quantities are dimensionless.

Define now the slip for the case with the bumps as $x_{s_b} = x_{0_b} - x_{h_b}$. After some algebra, we find

$$x_{s_b} = x_{s_{nb}} + \int_{x_{h_b}(t)}^{x_{0_b}(t)} f(x)\,dx. \tag{7.7}$$

The latter equation shows that the difference of slip at time t between bumpy and smooth channels comes from the contribution of the 'volume' $\Delta x_s(t) = x_{s_b}(t) - x_{s_{nb}}(t)$ of the bump (integral) between the particles' P_0 and P_h horizontal positions under the bump at time t (recall $f(x)$ is the profile of the bump).

7.1.3. Slip difference for one bump

From the plots on figures 9(a) and 9(b), one observes that there is a region for which there is a non-zero slip difference between bumpy and smooth channels. In other words, there is an interval of time $t_1 \leqslant t \leqslant t_2$ for which such a difference of slip indeed occurs. In particular, there is an optimum time t_{opt} for which this slip difference is maximal (clearly visible on figure 9b).

Let us now look more precisely at this region where a difference of slip occurs. Suppose that the bump is centred around $1/2$ and disappears upstream for $0 \leqslant x \leqslant 1/2 - \delta/2$ and downstream for $1/2 + \delta/2 \leqslant x \leqslant 1$. Its influence is of length δ. Mathematically, it means that $f(x) \simeq 0$ for $0 \leqslant x \leqslant 1/2 - \delta/2$ and $1/2 + \delta/2 \leqslant x \leqslant 1$. Recall $x_{0_b}(t) > x_{h_b}(t)$ at all time t. If $x_{0_b}(t_{end}) \leqslant 1/2 - \delta/2$, then $x_{s_b}(t_{end}) \simeq x_{s_{nb}}(t_{end})$. The two points have not gone yet under the bump, they are before the bump. We encounter no-slip difference. If $x_{h_b}(t_{end}) \geqslant 1/2 + \delta/2$, then also $x_{s_b}(t_{end}) \simeq x_{s_{nb}}(t_{end})$. The two points have both already gone past the bump. We encounter no-slip difference. It is now natural to define the two following times t_1 and t_2 given by $x_{0_b}(t_1) = 1/2 - \delta/2$ and $x_{h_b}(t_2) = 1/2 + \delta/2$ (see figure 10). Further algebra leads to

$$t_1 = \frac{1 - \delta}{1 - h^2(0)(1 - \Lambda^{-1})}, \tag{7.8}$$

$$t_2 = \frac{1 + \delta - 2\int_{(1-\delta)/2}^{(1+\delta)/2} f(x)\,dx}{1 - h^2(0)}. \tag{7.9}$$

7.1.4. Slip difference for N bumps

The microchannels used by Liau et al. (2005) present an alternation of half-cycles with each one containing N bumps in a row ($N = 10$). In other words, each half-cycle
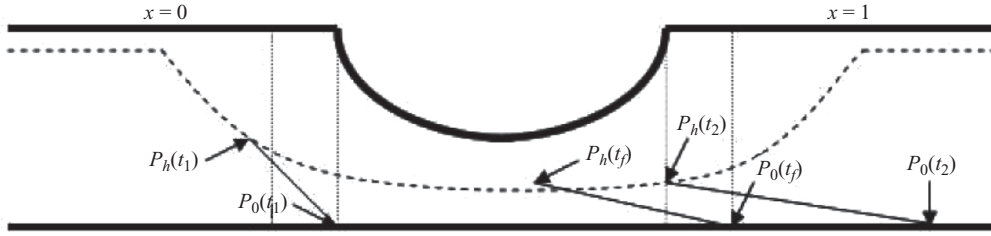
FIGURE 10. Sketch of the evolution of the slip in the case of a plug flowing in a bumpy channel. For simplicity, plugs are not represented and only the half-width of the channel is sketched. The interface between the two fluids A and B is represented by the dashed line. The solid lines link particles P_0 and P_h. At time t_1, particle P_0 is reaching the bump. At time t_2, particle P_h is leaving the bump. At time t_f, particle P_0 is reaching the end of the unit. Recall that a unit is defined by a dimensionless horizontal length of 1.

contains N unit cells with each one of them containing a bump. In the case of smooth serpentine channels, each half-cycle contains N unit cells too, but each one of them is a smooth channel. The so-called 'unit' has a dimensionless length of 1 or a dimensional length of $1/N$th the length of the half-cycle. Define t_f as the time the plug needs to go through a unit (see figure 10). In other words, t_f is given by $x_{0_b}(t_f) = 1$. The previous analysis shows that we need to have $t_1 \leqslant t_f \leqslant t_2$ in order to have a slip difference between the case with bumps and the case without bumps. Hence, providing $t_1 \leqslant t_f \leqslant t_2$, we have a significant difference between the slips for bumpy and smooth channels at the end of a unit given by

$$\Delta x_s(t_f) = \int_{x_{h_b}(t_f)}^{x_{0_b}(t_f)} f(x)\,dx \tag{7.10}$$

with $x_{0_b}(t_f)$ and $x_{h_b}(t_f)$ given by the transcendental expressions:

$$x_{h_b}(t_f) - \int_0^{x_{h_b}(t_f)} f(x)\,dx = \frac{1 - h^2(0)}{2}t_f, \tag{7.11}$$

$$x_{0_b}(t_f) - \int_0^{x_{0_b}(t_f)} f(x)\,dx = \frac{1 - h^2(0)(1 - \Lambda^{-1})}{2}t_f. \tag{7.12}$$

In the following analysis, we will compose N times the slip difference obtained through (7.10). The dimensionless time t_f needed for the particle P_0 to go through one bumpy unit is

$$t_f = 2(1 - h^2(0)(1 - \Lambda^{-1}))^{-1}\left(1 - \int_0^1 f(x)\,dx\right).$$

If we choose $h(0) = 0.90$, $\Lambda = 0.24$, $a = 0.7$ and $b = 20$, we obtain the dimensionless time $t_f \sim 0.41$, for example. Now look at the slip differences given by a single bump and N closely spaced bumps. The latter results can be seen on figure 11. The comparison between the two plots suggests that a non-zero slip difference occurs as long as the plug has not gone past the bump or the set of bumps. The new insight one obtains from these plots is quite remarkable. Mixing will be enhanced by bumps on the walls of the serpentine channel if the bumps are sufficiently close to each other (suggested by figure 11a) but also if the alternation of half-cycles (each half-cycle contains N bumps) is sufficiently closely spaced one to the next before the slip difference decays to zero (as shown on figure 11b). When these things are true, the reorientation step (see below) takes place before the slip difference relaxes to zero. This is the key insight.
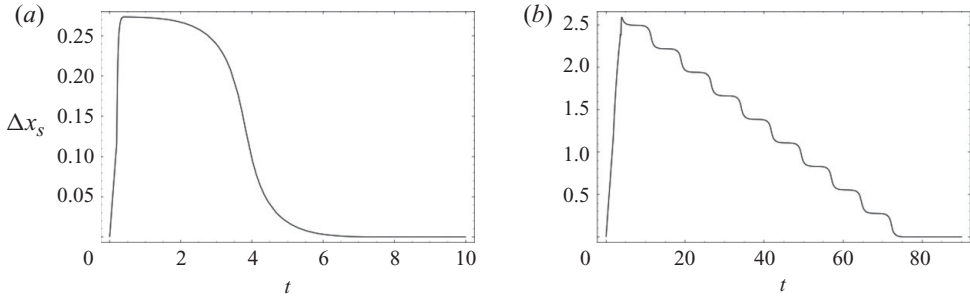
FIGURE 11. Slip difference $\Delta x_s(t) = x_{s_b}(t) - x_{s_{nb}}(t)$ for (*a*) 1 bump and (*b*) N bumps in a row. In (*b*), the bumps are closely spaced enough that the slip difference does not relax to 0 before the next bump in the sequence. All quantities are dimensionless.

7.2. *An optimization problem*

Note we can find an optimum time t_{opt} (figure 9*b*) given by the maximization of $\Delta x_s(t) = \int_{x_{h_b}(t)}^{x_{0_b}(t)} f(x)\,\mathrm{d}x$, where f is the prescribed wall profile. Consequently, the mixing will be enhanced when $t_f = t_{opt}$, in other words when the parameters $h(0)$, Λ and f are chosen accordingly. The parameters to be adjusted are the viscosity ratio Λ, the thickness of the lubrication layer through $h(0)$, the geometry of the bump through f (for a Gaussian, the parameters of the amplitude a and the standard deviation b). Also, the shape of the plug would eventually need to be taken into account through the parameter $k = \tilde{r}/\tilde{L}$. k is here the ratio of the radius of the plug over the distance between adjacent bumps in the channel. The latter parameter certainly is related to the time t_f required to go past one bump. For brevity, we do not include the parameter k in our analysis here. The study of this optimization problem is largely left for future work. In the meantime, we refer the reader to previous computational work done by Muradoglu & Stone (2005) who quantified the influence of various parameters on the mixing within droplets in the case of a smooth serpentine channel.

7.3. *Shear flow analysis*

We interpret the flow (with geometry sketched in figure 2) as a time-dependent shear flow where the magnitude of the net shear is given by the slip $x_s(t)$. We are working here in coordinates moving downstream with $x_0(t)$. The dimensionless deformation of the continuum is approximated by

$$\begin{cases} x_1 = X_1 - x_s(t)X_2, \\ x_2 = X_2, \end{cases} \tag{7.13}$$

where $(x_1(0), x_2(0)) = (X_1, X_2)$, X_1 and X_2 are constants. The displacement is given by

$$\begin{cases} \xi_1 = -x_s(t)X_2, \\ \xi_2 = 0. \end{cases} \tag{7.14}$$

Recall t_f is the time needed to go through one bump. After one bump then, the displacement $(\xi_1(t_f), \xi_2(t_f))$ is obtained. Compose N bumps in a row, the ensuing displacement is $\boldsymbol{u}(N) = -Nx_s(t_f)X_2\boldsymbol{E}_1$. Define the displacement gradient tensor $\boldsymbol{H}(N) = \partial \boldsymbol{u}/\partial \boldsymbol{X}$ which is here computed as

$$\boldsymbol{H}(N) = -Nx_s(t_f)\boldsymbol{E}_1 \otimes \boldsymbol{E}_2. \tag{7.15}$$
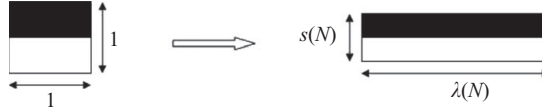
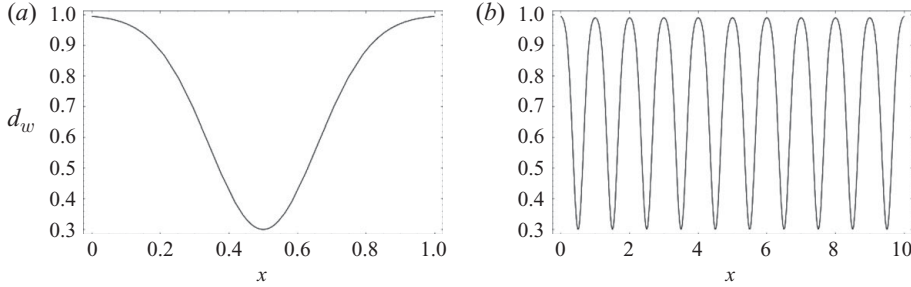FIGURE 12. A square of unit area of two segregated fluids after the passage through N units.

FIGURE 13. Bumpy wall profiles for (*a*) approach 1 with one bump prescribed by the profile $f(x)$; (*b*) approach 2 with N bumps prescribed by the profile $H(x)$. All quantities are dimensionless.

The finite strain tensor for the deformation in matrix form is

$$(\boldsymbol{E}(N)) = \begin{bmatrix} 0 & -Nx_s(t_f) \\ -Nx_s(t_f) & N^2x_s^2(t_f) \end{bmatrix}. \tag{7.16}$$

Now look at the stretching of a line element in the flow. For this purpose, we take a vector $\boldsymbol{M}$ such that $\|\boldsymbol{M}\| = 1$ and transform it into the vector $\lambda(N)\boldsymbol{m}$ of magnitude $\lambda(N)$. The stretching $\lambda_S(N)$ is given by $\lambda_S^2(N) = \max\{1 + 2\boldsymbol{M}\cdot\boldsymbol{E}(N)\boldsymbol{M}, \boldsymbol{M} \in \Re^2, \|\boldsymbol{M}\| = 1\}$. It corresponds to the maximal eigenvalue of $\boldsymbol{E}(N)$. The calculation gives

$$\lambda_S(N) = \frac{1}{\sqrt{2}}\left[2 + N^2x_s^2(t_f) + Nx_s(t_f)(N^2x_s^2(t_f) + 4)^{1/2}\right]^{1/2}. \tag{7.17}$$

We assume that when N bumps are in a row in a half-cycle of the serpentine, they participate only in the shear-induced stretching of the flow (Ottino & Wiggins 2004; Sturman *et al.* 2006) and not in reorientation. The conservation of mass principle (sketched on figure 12) gives after N bumps:

$$\lambda_S(N)s(N) = 1, \tag{7.18}$$

where $s(N)$ is the striation thickness obtained after N bumps. Hence,

$$s(N) = \sqrt{2}\left[2 + N^2x_s^2(t_f) + Nx_s(t_f)(N^2x_s^2(t_f) + 4)^{1/2}\right]^{-1/2}. \tag{7.19}$$

A similar analysis for a smooth serpentine channel with a different $x_s(t_f)$ would give a different $s(N)$ after N smooth units.

7.4. *Comparison of the true slip versus stretch from the composite finite strain tensor*

We compare our approach used so far, named approach 1 in the following, with another approach named approach 2 (see figure 13). Approach 2 consists of determining the slip between particles P_0 and P_h after the latter particles have gone past N bumps. We compare the slip obtained with the composition of N bumps used so far giving the following slip $x_{s_1}(t) = Nx_s(t)$. We name $H(x)$ the wall profile corresponding to the assembly of N bumps in a row (figure 13*b*) so that

$d_w(x) = 1 - H(x)$. This time, for approach 2, $x \in [0, N]$. Following the same routine as for approach 1, we determine the difference of slip between bumps and no bumps for approach 2 and find

$$x_{S_{b_2}} = x_{S_{nb_2}} + \int_{x_{h_b}(t)}^{x_{0_b}(t)} H(x)\,\mathrm{d}x. \tag{7.20}$$

If by analogy with approach 1, we now call T_f the time to compose the N bumps with the approach 2, we have

$$x_{S_{b_2}} = x_{S_{nb_2}} + \int_{x_{h_b}(T_f)}^{x_{0_b}(T_f)} H(x)\,\mathrm{d}x. \tag{7.21}$$

Note also that

$$x_{0_b}(t) - \int_0^{x_{0_b}(t)} H(x)\,\mathrm{d}x = \frac{1 - h^2(0) + \Lambda^{-1}h^2(0)}{2}t, \tag{7.22}$$

$$x_{h_b}(t) - \int_0^{x_{h_b}(t)} H(x)\,\mathrm{d}x = \frac{1 - h^2(0)}{2}t. \tag{7.23}$$

Therefore $x_{0_b}(T_f) = N$ leads to the following time T_f:

$$T_f = 2\left(N - \int_0^N H(x)\,\mathrm{d}x\right)/(1 - h^2(0) + \Lambda^{-1}h^2(0)). \tag{7.24}$$

Note that by construction $\int_0^N H(x)\,\mathrm{d}x \sim N \int_0^1 f(x)\,\mathrm{d}x$ so that we have $T_f \sim N t_f$. Now, by comparing approaches 1 and 2,

$$x_{s_1} - x_{s_2} = \int_0^{x_{h_b}(Nt_f)} H(x)\,\mathrm{d}x - N \int_0^{x_{h_b}(t_f)} f(x)\,\mathrm{d}x, \tag{7.25}$$

which can also be seen as

$$x_{s_1} - x_{s_2} = x_{h_b}(Nt_f) - Nx_{h_b}(t_f). \tag{7.26}$$

Numerically, the difference between the two approaches, evaluated through (7.26) is small. Indeed for $N = 10$, we find $(x_{s_1} - x_{s_2})/x_{s_1} \sim 0.02$. The latter result confirms the legitimacy of our approach 1 used thus far. In other words, it is a fine approximation to compose the effects of single bumps when considering the net shear due to flow past a set of bumps.

7.5. *Asymmetric bump*

For completeness, we note the following. In the case where we have two Newtonian fluids and the bump is asymmetric (figure 14a), we find that sufficiently long after the plug has gone past the bump, we have no difference in slips between the case with bumps and the case with no bumps. The reason is straightforward as even when there is a change in symmetry properties in the bump profile, the line integral,

$$\Delta x_s(t) = \int_{x_{h_b}(t)}^{x_{0_b}(t)} f(x)\,\mathrm{d}x,$$

still holds.

7.6. *The transfer of shear stress to a non-Newtonian inner fluid.*

This work is presented in detail in Appendix B. We find here that the slip difference between bumpy and smooth mixers can be made persistent (rather than evanescent)
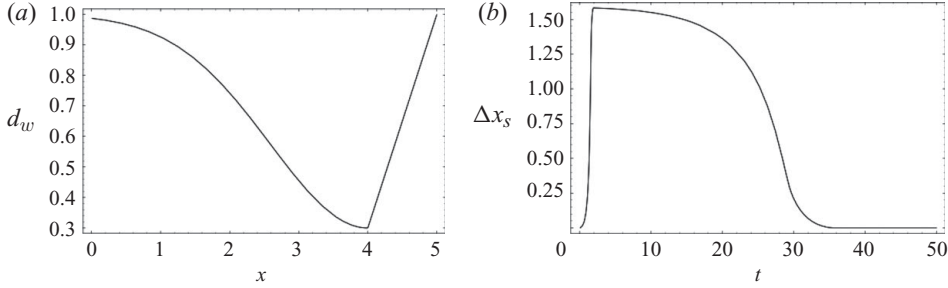
FIGURE 14. (*a*) Asymmetric bump profile. (*b*) Slip difference between bumps and no bumps in the case of an asymmetric bump profile. All quantities are dimensionless.

by changing the rheology of the interior fluid, e.g. from Newtonian to non-Newtonian. Indeed, we show that the particle P_h accelerates less than the particle P_0 under the bump for a shear-thinning fluid whereas the particle P_h accelerates more than the particle P_0 under the bump for a shear-thickening fluid. For a Newtonian fluid, the particle P_h accelerates as much as the particle P_0 under the bump.

8. Transfer of shear stress to the inner fluid in the presence of insoluble surfactants

In the foregoing section (with details in Appendix B), we saw that one way to affect the intensity of advection caused by a bump is through a change in rheology of fluid A to non-Newtonian. In this section, we show another way is through the effects of a surfactant on the A–B interface.

8.1. *Interfacial transport equation*

For a surfactant of surface concentration at the interface A–B, we have the interfacial transport equation (Edwards, Brenner & Wasan 1991)

$$\frac{\partial \tilde{\Gamma}}{\partial \tilde{t}} + \tilde{\boldsymbol{\nabla}}_S \cdot [\tilde{\Gamma} \tilde{\boldsymbol{u}}_h] = \tilde{D}_S \tilde{\nabla}_S^2 \tilde{\Gamma} + \tilde{D}(\tilde{\boldsymbol{\nabla}}\tilde{C}) \cdot \boldsymbol{e}_{\tilde{n}}(\tilde{y} = \tilde{h}(\tilde{x})), \tag{8.1}$$

where $\tilde{\Gamma}$ is the surface-excess of surfactant at the interface A–B, $\tilde{C}$ is the bulk concentration of surfactant in fluid A, $\tilde{D}_S$ is the diffusion coefficient of surfactant on the interface A–B, $\tilde{D}$ is the diffusion coefficient of surfactant in the bulk fluid A. We use dimensionless quantities from $\tilde{\Gamma} = \tilde{\Gamma}_0 \Gamma$, $\tilde{C} = \tilde{C}_0 C$, $\tilde{u}_h = \tilde{U} u_h$, $\tilde{v}_h = \epsilon \tilde{U} v_h$, $\tilde{h} = \tilde{d} h$, $\tilde{x} = \tilde{L} x$, $\tilde{y} = \tilde{d} y$, $\tilde{t} = \tilde{\tau} t$ to derive the dimensionless transport equation:

$$\frac{\partial \Gamma}{\partial t} + \frac{\partial}{\partial x}[\Gamma u_h] + \epsilon^2 \frac{\partial}{\partial x}[\Gamma v_h]\frac{\mathrm{d}h}{\mathrm{d}x} = \frac{1}{Pe_s}\frac{\partial^2 \Gamma}{\partial x^2}\left(1 + \epsilon^2\left(\frac{\mathrm{d}h}{\mathrm{d}x}\right)^2\right)$$
$$- \frac{\epsilon\beta}{Pe}\frac{\mathrm{d}h}{\mathrm{d}x}\frac{\partial C}{\partial x}(y = h(x)) + \frac{\beta}{\epsilon Pe}\frac{\partial C}{\partial y}(y = h(x)), \tag{8.2}$$

where $\tilde{\tau} = \tilde{L}/\tilde{U} = \tilde{d}/(\tilde{U}\epsilon)$, $Pe_s = (\tilde{U}\tilde{L})/\tilde{D}_S = (\tilde{U}\tilde{d})/(\epsilon\tilde{D}_S)$, $Pe = (\tilde{U}\tilde{d})/\tilde{D}$ and $\beta = (\tilde{d}\tilde{C}_0)/\tilde{\Gamma}_0$. As done previously, we drop the terms of orders ϵ^2 and ϵ^3 in (8.2):

$$\epsilon\frac{\partial \Gamma}{\partial t} + \epsilon\frac{\partial}{\partial x}[\Gamma u_h] = \frac{\epsilon}{Pe_s}\frac{\partial^2 \Gamma}{\partial x^2} - \frac{\beta}{Pe}\frac{\partial C}{\partial y}(y = h(x)). \tag{8.3}$$

Now consider a steady regime and the case of insoluble surfactants ($C=0$), the interfacial transport equation simplifies to the gathering of the following terms of the same magnitude of order ϵ:

$$\frac{\mathrm{d}}{\mathrm{d}x}[\Gamma u_h] = \frac{1}{Pe_s}\frac{\mathrm{d}^2\Gamma}{\mathrm{d}x^2}. \tag{8.4}$$

8.2. Elasticity relation

Close to equilibrium and for dilute surfactant solutions, the dimensionless surface tension gradient can be linearly correlated to the dimensionless surfactant concentration gradient at the interface (Edwards *et al.* 1991; Eggleton, Pawar & Stebe 1999):

$$\nabla_S\gamma = -\alpha E\nabla_S\Gamma, \tag{8.5}$$

where E is the elasticity parameter of the surfactant and $\alpha = \tilde{\Gamma}_{eq}/\tilde{\Gamma}_\infty$ is the fraction of the interfacial area that is initially covered by surfactant. $\tilde{\Gamma}_{eq}$ is the excess surfactant density on the surface A–B at equilibrium and $\tilde{\Gamma}_\infty$ is the upper bound of surfactant concentration. We transform the elasticity relation (8.5) into dimensionless form $\mathrm{d}\gamma/\mathrm{d}x = -\alpha E\mathrm{d}\Gamma/\mathrm{d}x$ and obtain the following dimensionless stress balance:

$$\frac{\partial u_B}{\partial y}(x,h(x)) - \Lambda\frac{\partial u_A}{\partial y}(x,h(x)) = \epsilon E_l\frac{\mathrm{d}\Gamma}{\mathrm{d}x}, \tag{8.6}$$

where $E_l = \alpha E/Ca$. The parameter $\epsilon_{E_l} = \epsilon\alpha E/Ca$ appears as a new relevant dimensionless group. Following our previous analysis, three distinct cases are to be explored in terms of the values of the parameter ϵ_{E_l}. Case I. When $\epsilon_{E_l} \ll 1$, the surface tension on the interface plays a subdominant role. The latter case has been studied in the previous part. Case II. When $\epsilon_{E_l} \sim 1$, the surface tension at the interface does have a significant influence. This is the case we intend to address in this part. Case III. When $\epsilon_{E_l} \gg 1$, the scaling used so far in our lubrication approximations is not valid anymore. Literature data (Eggleton *et al.* 1999) give the following order of magnitude for the elasticity parameter $E \sim 0.2$, which leads to values of ϵ_{E_l} ranging from 0.07 to 0.7.

We introduce the dimensionless group ϵ_{E_l} and obtain the following horizontal velocity fields:

$$u_A(x,y) = -\frac{1}{2\Lambda}\frac{\mathrm{d}p}{\mathrm{d}x}[h^2(x)-y^2] + \frac{1}{2}\frac{\mathrm{d}p}{\mathrm{d}x}\left[h^2(x)-d_w^2(x)\right] + \epsilon_{E_l}\frac{\mathrm{d}\Gamma}{\mathrm{d}x}\left[h(x)-d_w(x)\right], \tag{8.7}$$
$$0 \leqslant x \leqslant 1, \qquad 0 \leqslant y \leqslant h(x),$$

$$u_B(x,y) = -\frac{1}{2}\frac{\mathrm{d}p}{\mathrm{d}x}\left[y^2-d_w^2(x)\right] + \epsilon_{E_l}\frac{\mathrm{d}\Gamma}{\mathrm{d}x}\left[y-d_w(x)\right], \tag{8.8}$$
$$0 \leqslant x \leqslant 1, \qquad h(x) \leqslant y \leqslant d_w(x).$$

8.3. Numerical solutions

We look at the solution $\{p(x), h(x), \Gamma(x)\}$ for a wall profile prescribed as a Gaussian function $d_w(x) = 1 - ae^{-b(x-1/2)^2}$ (figure 5a). To obtain the solution, we solve the Reynolds lubrication equations for fluids A and B, coupled to the interfacial transport equation (see Appendix A for details). To facilitate the calculations, the interfacial transport equation is integrated as

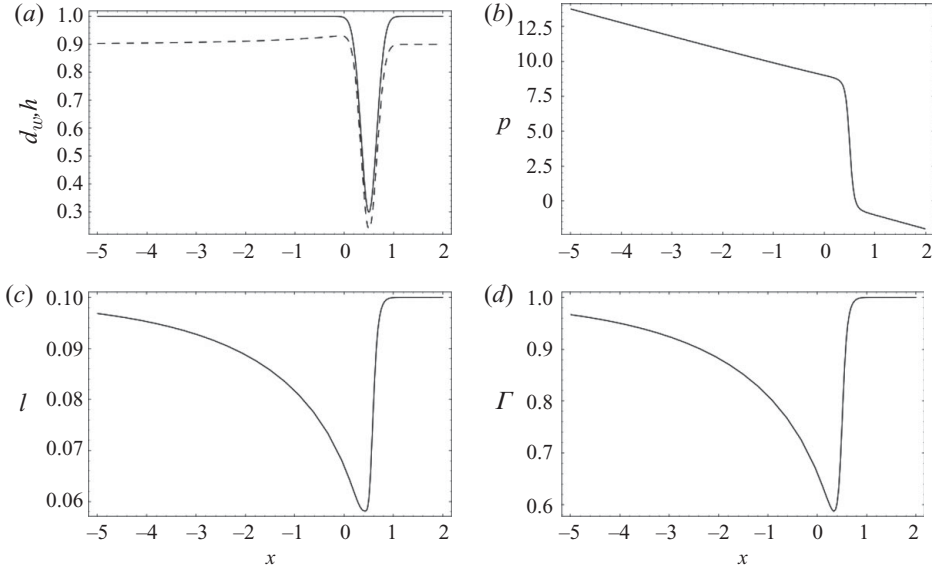$$\Gamma(x)u_h(x) = \frac{1}{Pe_s}\frac{\mathrm{d}\Gamma}{\mathrm{d}x} + \Gamma(\infty)u_h(\infty), \tag{8.9}$$

FIGURE 15. (*a*) Wall $d_w(x)$ and interface $h(x)$ (dashed) profiles. (*b*) Pressure profile $p(x)$ in the channel. (*c*) Lubrication layer thickness $l(x)$ in the channel. (*d*) Surfactant concentration $\Gamma(x)$ at the interface A–B along the channel. All quantities are dimensionless.

where we assumed that the surfactant gradient is negligible at infinity. If we look at the interfacial transport equation (8.9) in more detail, we can study two limiting cases. Firstly, we assume $1/Pe_S$ is large, in other words we have attained the diffusion limit. Then, (8.9) simplifies to $\mathrm{d}\Gamma/\mathrm{d}x = 0$. If we prescribe the boundary condition $\Gamma(0) = 1$, we obtain $\Gamma(x) = 1$ all along the channel. We have come back to the case of constant interfacial tension studied previously. Secondly, we assume that $1/Pe_S$ is small, in other words we have attained the convection limit and obtain the simplified version of (8.9):

$$\Gamma(x)u_h(x) = \Gamma(\infty)u_h(\infty). \tag{8.10}$$

Therefore a maximum in the interfacial velocity profile corresponds to a minimum in the interfacial surfactant concentration. Also, we can infer trivially from (8.10) that the product $\Gamma(x)u_h(x)$ is even with respect to the location of the bump in the middle of the channel. However, this does not mean though that each one of Γ and u_h is symmetric with respect to the location of the bump.

8.4. *Convection limit*

The numerical solutions for interface profile, pressure, lubrication layer thickness and surfactant concentration at the interface A–B are plotted in (see figure 15) for $h(0) = 0.90$, $\Lambda = 0.24$, $a = 0.7$, $b = 20$, $\tilde{D}_S = 10^{-10}$ m^2 s^{-1}. The choice of parameters is intended to be suggestive of the experimental conditions. We shall set $\epsilon_{E_l} = 1$ so that the Poiseuille part of the flow field and the Marangoni stresses are of the same order of magnitude. Also, we have attained here the convection limit as $Pe_S = 10^5$.

As in the case of no insoluble surfactants at the interface, under the bump at $x = 0.50$, there is an inflexion point for the pressure profile. But, at the same time, the presence of the bump at $x = 0.50$ delocalizes the other extrema. The surfactant concentration and the lubrication layer thickness present minima around $x = 0.34$. The horizontal velocity at the interface $y = h(x)$ (figure 16*c*) presents a maximum at
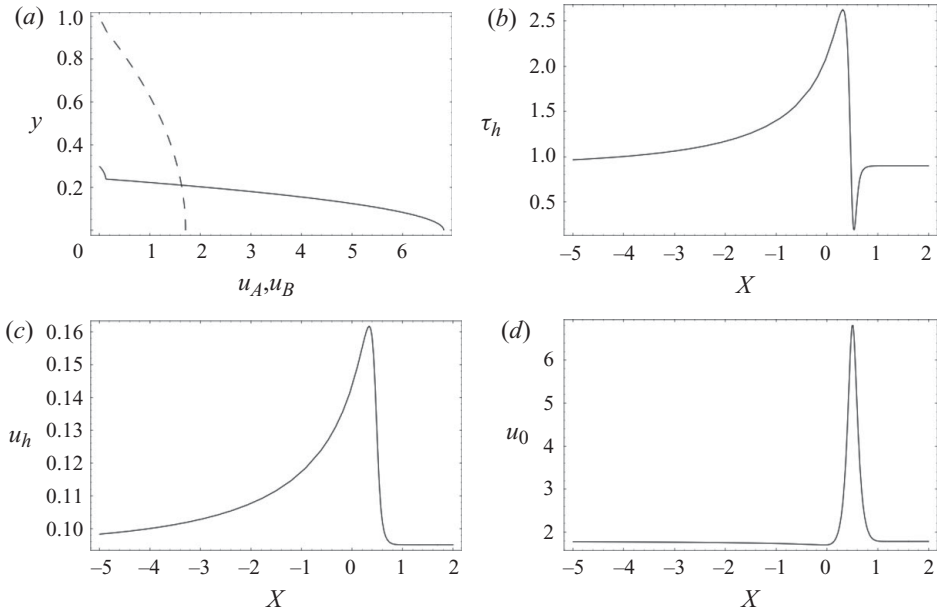
FIGURE 16. (a) Horizontal velocity profiles far (dashed) and under the bump. (b) Shear stress at the interface between the two fluids along the channel. (c) Horizontal velocity u_h at the interface $y = h(x)$ along the channel. (d) Horizontal velocity u_0 in the middle of the channel at $y = 0$ along the channel. All quantities are dimensionless.

the same location as the location of the minimum of the surfactant concentration. The shear stress (figure 16b) presents a maximum around $x = 0.31$ and a minimum around $x = 0.53$. Meanwhile, there is a maximum for the horizontal velocity at $y = 0$ (figure 16d) under the bump ($x = 0.50$). Quantitatively, the interfacial shear stress presents a maximum of about 2.6 times more as compared with far from the bump and a minimum of about 5.8 times less as compared with far from the bump this time.

8.5. Transition from diffusion limit to convection limit

We see a transition from the diffusion limit to the convection limit as the interfacial diffusivity $\tilde{D}_S$ is decreased. Surfactant gradients or Marangoni stresses start to appear when $1/Pe_S$ changes from superior to 1 to inferior to 1. This is confirmed numerically in the previous calculations as the surfactant concentration profile $\Gamma(x)$ changes from a 'diffusive' profile to a 'convective' profile when $\tilde{D}_S \sim 10^{-5}$ m^2 s^{-1}. In other words, we see Marangoni stresses and a significant influence of insoluble surfactants for interfacial diffusion coefficients $\tilde{D}_S$ lower than 10^{-5} m^2 s^{-1}. The literature (Chang & Franses 1995) gives the following order of magnitude for $\tilde{D}_S$: $\tilde{D}_S \sim 10^{-10}$ m^2 s^{-1}. We are then in the convection limit.

8.6. Influence of the elasticity parameter E

Once we have reached the convection limit, there is an influence of the surfactants on the flow. We now study the influence of the parameters E and α on the flow. In the previous calculations, we have chosen $\epsilon_{E_l} = 1$ so that the order of magnitude of the Marangoni stresses can be the same as the order of magnitude of the Poiseuille part of the flow. If we have $\epsilon_{E_l} \sim 0.1$ or of lower order of magnitude, then the influence of surfactants on the flow and consequently on the mixing becomes negligible. If we

Perfluorinated surfactant addition	1:10	1:5	1:2
Hb concentration (mg ml^{-1})	35	35	35
Λ	0.24	0.24	0.24
Interfacial surface tension (mN m^{-1})	3.47 ± 0.47	3.76 ± 0.56	3.18 ± 0.43
Ca	0.12	0.11	0.13
Number of half-cycles M for full mixing in bumpy channel (experimental)	4	10	10

TABLE 3. Experimental results obtained for samples of $35\,\text{mg ml}^{-1}$ Hb with different concentrations of insoluble surfactants in the oil carrier fluid with flow rates of $2\,\mu\text{l min}^{-1}$ for the oil stream and $0.2\,\mu\text{l min}^{-1}$ for Hb streams. The viscosity of the oil carrier is supposed to be invariant with the insoluble surfactant concentration: we keep $\tilde{\mu}_B = 4.88\,\text{mPa s}$.
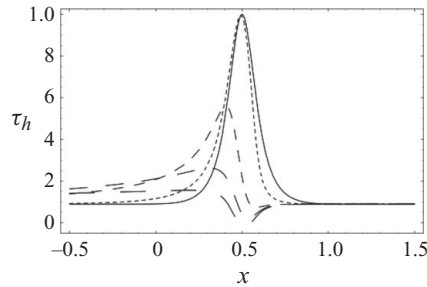

FIGURE 17. Interfacial shear stress with (dashed) or without (solid, i.e. $\epsilon_{E_l} = 0$) insoluble surfactants for different values of the parameter ϵ_{E_l}. The larger the dashes the greater the value of ϵ_{E_l}. We have chosen $\epsilon_{E_l} \in \{0.1; 0.5; 1; 2\}$ and also $h(0) = 0.90$, $\Lambda = 0.24$, $a = 0.7$, $b = 20$, $D_S = 10^{-10}\,\text{m}^2\,\text{s}^{-1}$. All quantities are dimensionless.

have $\epsilon_{E_l} \sim 1$ or of higher order of magnitude, then the influence of surfactants on the flow and consequently on the mixing becomes significant. One should pay attention here not to go too high in the parameters E and α otherwise the scaling $\epsilon_{E_l} \sim 1$ will be violated and our lubrication approximations so far used will not be valid anymore.

Figure 17 clearly shows the influence of the surfactants on the interfacial shear stress. The insoluble surfactants both diminish the amplitude of the interfacial shear stress and delocalize the maximum of the interfacial shear stress from under the bump ($x = 0.50$) to upstream of the bump. The more 'elastic' the surfactant is, the more the interfacial shear stress under the bump is reduced or even transformed into a minimum under the bump (see figure 17). As a conclusion, insoluble surfactants have a significant influence on the mixing only for values of the parameter $\epsilon_{E_l} \geqslant 1$. They diminish mixing for the approximate range $0.1 \leqslant \epsilon_{E_l} \leqslant 2$. As ϵ_{E_l} increases, there is a longer patch of elevated shear before bump.

8.7. *Comparison with experimental data*

Table 3 shows that increasing the surfactant addition in the oil carrier stream diminishes the mixing in bumpy channels. This is what the comparison of 1:5 and 1:2 surfactant data with 1:10 surfactant data suggests. The comparison of 1:5 surfactant and 1:2 surfactant data suggests that the interface has reached saturation. Recall that $\epsilon = 10/24 \sim 0.42$ (from the channel dimensions $\tilde{L} = 24\,\mu\text{m}$ and $\tilde{d} = 10\,\mu\text{m}$, which implies bumps sufficiently close to each other), so that we obtain $\epsilon/Ca \sim 3.5$ and $\epsilon E/Ca \sim 0.7$ for all three experiments. ϵ_{E_l} will now depend on α. In the saturation case, $\alpha \sim 0.99$ so that $\epsilon_{E_l} \sim 0.69$, which puts in the range where insoluble surfactants
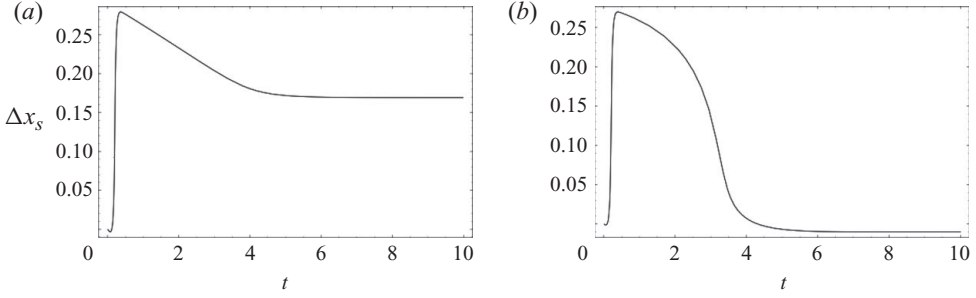
(a)

(b)

FIGURE 18. Slip difference $\Delta x_s(t) = x_{s_b}(t) - x_{s_{nb}}(t)$ between bumps and no bumps in the case of insoluble surfactants at the interface between the two fluids for (a) $\epsilon_{E_l} = 2$, (b) $\epsilon_{E_l} = 0.1$. Note that $t = 0$ corresponds to $x_h(0) = 0$ and $x_0(0) = 0$ here. All quantities are dimensionless.
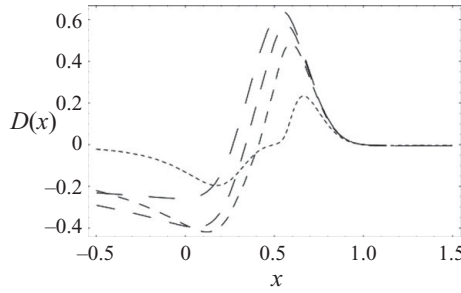

FIGURE 19. $D(x)$ in the case of insoluble surfactants at the interface between the two fluids. The larger the dashes the greater the value of ϵ_{E_l}. We have chosen $\epsilon_{E_l} = \{0.1; 0.5; 1; 2\}$ and also $h(0) = 0.90$, $\Lambda = 0.24$, $a = 0.7$, $b = 20$, $D_S = 10^{-10}$ m^2 s^{-1}. All quantities are dimensionless.

have an influence on mixing in the sense that they diminish mixing. In the 1:10 surfactant case, we can imagine that α is small enough, say perhaps $\alpha \sim 0.1$ so that the influence of insoluble surfactants ($\epsilon_{E_l} \sim 0.07$) on the mixing becomes negligible. More experimental work would be valuable to explore these interesting phenomena.

Coming back to the framework exposed by (B.16) (see Appendix B), in the case of insoluble surfactants at the interface of two Newtonian fluids, we have

$$G(x) = \frac{1}{4\Lambda} \left[\left(\frac{dp}{dx}\right)_\infty \left(\frac{dp}{dx}\right) \left[h_\infty^2 d_w^2 - h^2 d_{w_\infty}^2\right] \right]$$
$$+ \frac{\epsilon_{E_l}}{2\Lambda} \left[\left(\frac{dp}{dx}\right)_\infty \left(\frac{d\Gamma}{dx}\right) h_\infty^2 (d_w - h) \right] - \frac{dp}{dx} \left(\frac{d\Gamma}{dx}\right)_\infty h^2 (d_{w_\infty} - h_\infty). \quad (8.11)$$

If, in addition, we assume $(d\Gamma/dx)_\infty = 0$, we then obtain the following:

$$G(x) = \frac{1}{4\Lambda} \left(\frac{dp}{dx}\right)_\infty \frac{dp}{dx} \left[h_\infty^2 d_w^2 - h^2 d_{w_\infty}^2\right] + \frac{\epsilon_{E_l}}{2\Lambda} \left(\frac{dp}{dx}\right)_\infty \frac{d\Gamma}{dx} h_\infty^2 (d_w - h). \quad (8.12)$$

After sufficiently long times after the plug has gone past the bump, the slip difference between bumps and no bumps reaches a plateau (see figure 18).

We now look at $\Delta x_s(t)$ and $D(x) = (u_h(\infty)/u_h(x)) - (u_0(\infty)/u_0(x))$ with respect to ϵ_{E_l} (see figures 18 and 19). We see that the interfacial velocity accelerates less under the bump when the strength of interfacial surfactants increases. In other words, interfacial surfactants decrease the interfacial velocity which results into a positive non-zero slip difference.

9. Future work

Surface tension measurements have shown that the insoluble surfactants used in the experiments do not have a strong influence on the interfacial tension (see table 1). Therefore, we suspect that changes of interfacial tension are due to adsorption of the crowding agents BSA and Hb at the interface. Consequently, it will be interesting to consider soluble surfactants in the problem. Indeed, we suspect that adsorption of crowding agents at the interface strongly affects the mixing. Consideration of adsorption of crowding agents will involve studying the bulk transport equation in solution of Newtonian fluid A and requires the introduction of a supplementary dimensionless unknown bulk concentration of soluble surfactant C. In the same time, it modifies the dimensionless interfacial transport equation with the addition of flux terms. A solution of this problem consists of $\{p(x), h(x), \Gamma(x), C(x, y)\}$ at steady state. The latter should satisfy the Reynolds lubrication equations for fluids A and B, the interfacial transport equation and the bulk transport equation. This will also require the introduction of boundary conditions for the bulk concentration C. In addition, the introduction of a kinetic condition or an equilibrium partition of the type Langmuir or Frumkin isotherm (Graham & Phillips 1979*a*,*b*) will be needed: it will relate the interfacial surfactant concentration and the bulk surfactant concentration. This problem of soluble surfactants remains for future work. A start is to use a cross-film average such as in Jensen & Grotberg (1999).

10. Conclusion

We have presented here an analysis of a simpler problem that confirms the experimental observations of mixing enhancement within drops in serpentine channels when bumps are present on the channel walls. Our analysis qualitatively confirms that the protrusions on the walls will enhance mixing in plugs of Hb and BSA. In addition, the analysis confirms that it is more difficult to mix non-Newtonian fluids such as BSA in such devices. The analysis also confirmed that the presence of insoluble surfactants tends to reduce mixing. Still, a broader field of investigations lies ahead as experiments suggest considerable adsorption of proteins at the oil–plug interface. Further analysis should include modelling the adsorption and desorption of proteins at the interface.

The keys to relating the flow in the long drops (in the experiments) to the infinite two-fluid channel flow we analysed are as follows. The pressure gradient modulation associated with interaction of a moving plug with the next bump factors out of our slip analysis. The analysis further focuses on the ratio of shear stress enhancement caused by the bump; the ratio is insensitive to the film thickness away from the bump, which quantity is determined by the mechanics at the leading edge of the plug. In this way, the analysis of the simpler flow captures the key mechanisms of the flows observed in the experiments.

Physically, this paper demonstrates that the thinning of the lubrication layer B at the bump enhances the shear stress at the interface and that increased shear stress at the interface leads to greater advection velocities in the interior fluid A. This is the basis for the enhancement of mixing. In addition, when the interior fluid is Newtonian, we have shown that mixing will be enhanced by bumps on the walls of the serpentine channel if the bumps are sufficiently close to each other but also if the alternation of half-cycles is sufficiently closely spaced one to the next. When these things are not true, the slip difference between bumpy and smooth channels relaxes to zero. Moreover, the slip difference between bumpy and smooth mixers can be made

BSA concentration		$10\,\mathrm{mg\,ml}^{-1}$	$50\,\mathrm{mg\,ml}^{-1}$
Λ		0.20	0.20
Number of half-cycles M for			
full mixing in bumpy channel (experimental)		7	9
Hb concentration		$10\,\mathrm{mg\,ml}^{-1}$	$35\,\mathrm{mg\,ml}^{-1}$
Λ		0.22	0.24
Number of half-cycles M for			
full mixing in bumpy channel (experimental)		3	4

TABLE 4. Experimental results obtained for samples of different BSA and Hb concentrations with flow rates of $2\,\mu\mathrm{l\,min}^{-1}$ for the oil stream and $0.2\,\mu\mathrm{l\,min}^{-1}$ for BSA/Hb streams.

persistent (rather than evanescent) by changing either the rheology of the interior fluid (from Newtonian to non-Newtonian for instance) or by modifying the structure of the interface (by populating it with insoluble surfactants, for example).

Appendix A. Boundary conditions implemented in Mathematica

For the cases of (a) two Newtonian fluids A and B and no surfactants, (b) one non-Newtonian fluid A, one Newtonian fluid B and no surfactants, we used the following boundary conditions: $h(0) = 0.90$, $p(0) = 1$, $p'(0) = -1$. Now, for the case of two Newtonian fluids A and B and insoluble surfactants at the interface, we used the following boundary conditions: $h(0) = 0.90$, $p(10) = -10$, $p'(10) = -1$, $\Gamma(10) = 1$, $\Gamma'(10) = 0$. In the latter case, we had to constrain the boundary conditions downstream so that Mathematica (Wolfram Research 2005) could solve the partial differential equations and allow for physically realistic results.

Appendix B. Transfer of shear stress to a non-Newtonian inner fluid

B.1. *Results*

Experimentally (see table 4), it has been shown it is harder to mix BSA (BSA) (non-Newtonian) than Hb (Newtonian) in bumpy channels. We qualitatively verify this empirical fact with our model.

We now assume that fluid A is non-Newtonian such as many crowding agents. In particular, BSA is shear thinning (Ikeda & Nishinari 2000). We consider the following power-law model (Bird, Armstrong & Hassager 1987) with $n = 0.1$ (Ikeda & Nishinari 2000) to describe its dimensional shear stress:

$$\tilde{\tau}_{\tilde{x}\tilde{y}_A} = \tilde{m} \left| \frac{\partial \tilde{u}_A}{\partial \tilde{y}} \right|^{n-1} \frac{\partial \tilde{u}_A}{\partial \tilde{y}}, \tag{B 1}$$

where $\tilde{m}$ and n are rheological constants for fluid A. The fluid B remains Newtonian in the following. We choose a power-law model rather than a Carreau model (Bird *et al.*
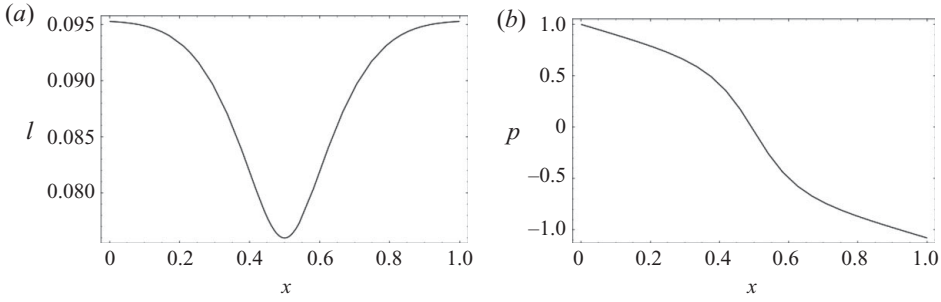
FIGURE 20. (a) Lubrication layer thickness $l(x) = d_w(x) - h(x)$ along the channel. (b) Pressure profile $p(x)$ in the channel. All quantities are dimensionless.

1987) to facilitate analysis. Also, due to the small dimensions of the channel, we expect high shear rates in the experiments. We solve the modified Navier–Stokes equations and assume $\mathrm{d}p/\mathrm{d}x < 0$. We obtain the dimensionless horizontal velocity fields:

$$u_A(x, y) = \left(-\frac{\mathrm{d}p}{\mathrm{d}x}\right)^{1/n} /((1/n + 1)\Lambda)[h^{1/n+1}(x) - y^{1/n+1}]$$

$$+ \frac{1}{2}\frac{\mathrm{d}p}{\mathrm{d}x}\left[h^2(x) - d_w^2(x)\right], \; 0 \leqslant x \leqslant 1, 0 \leqslant y \leqslant h(x), \quad (B2)$$

$$u_B(x, y) = \frac{1}{2}\frac{\mathrm{d}p}{\mathrm{d}x}\left[y^2 - d_w^2(x)\right], \; 0 \leqslant x \leqslant 1, h(x) \leqslant y \leqslant d_w(x), \quad (B3)$$

where $\Lambda = \tilde{m}/\tilde{\mu}_B(\tilde{U}/\tilde{d})^{n-1}$ is a dimensionless group representing a viscosity ratio between the two fluids. In order to apply our slip analysis, we examine the horizontal velocity fields at $y = 0$ and at the interface $y = h(x)$:

$$u_0(x) = \left(-\frac{\mathrm{d}p}{\mathrm{d}x}\right)^{1/n} /((1/n + 1)\Lambda)[h^{1/n+1}(x)] + \frac{1}{2}\frac{\mathrm{d}p}{\mathrm{d}x}\left[h^2(x) - d_w^2(x)\right], \quad (B4)$$

$$u_h(x) = \frac{1}{2}\frac{\mathrm{d}p}{\mathrm{d}x}\left[h^2(x) - d_w^2(x)\right]. \quad (B5)$$

We prescribe in our numerical simulations n and Λ (viscosity ratio), independently of the parameters contained in Λ. We look at the solution $\{p(x), h(x)\}$ for a wall profile prescribed as a Gaussian function $d_w(x) = 1 - a\mathrm{e}^{-b(x-1/2)^2}$ (see figure 5a) (see Appendix A for details). The numerical solutions for lubrication layer thickness and pressure are plotted in figure 20 for $h(0) = 0.90$, $\Lambda = 0.20$, $n = 0.1$, $a = 0.7$ and $b = 20$. The choice of parameters is intended to be suggestive of the experimental conditions. Results shown on figure 21 can be compared with the Newtonian results shown on figure 6.

As in the case of two Newtonian fluids (see figures 5 and 6), under the bump at $x = 1/2$, there is a thinning of the lubrication layer and an inflexion point for the pressure profile. A minimum in the wall profile under the bump leads also to a maximum in the shear stress (figure 21b). At the same time, it provides a maximum for the horizontal velocities at the interface $y = h(x)$ and at $y = 0$ (figure 21c,d). Physically, the thinning of the lubrication layer B under the bump still enhances the shear stress at the interface, certainly providing an enhanced mixing inside the plug, as in the case of two Newtonian fluids. Note though that the shapes of the fluid profiles
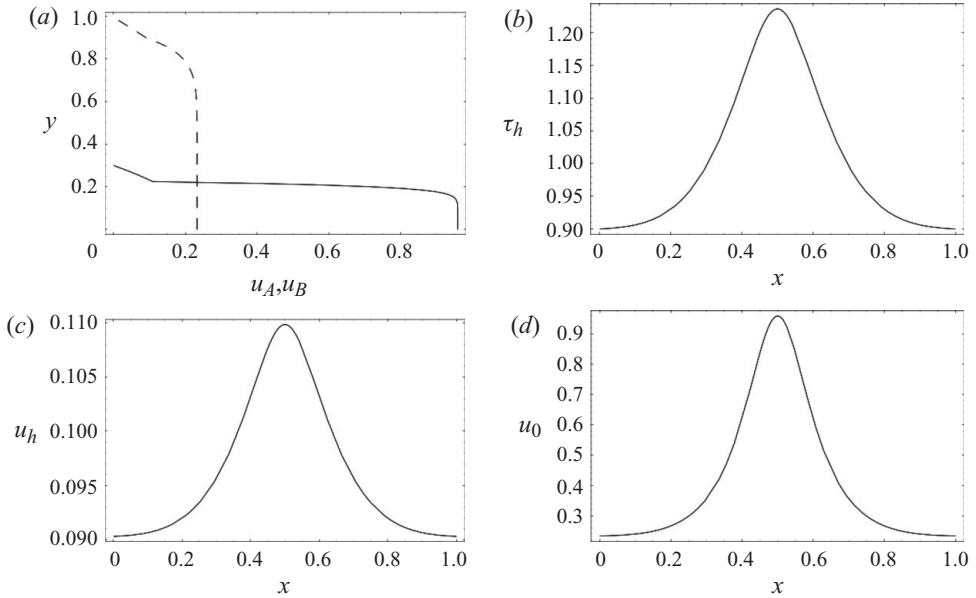
FIGURE 21. (*a*) Horizontal velocity profiles far from (dashed) and under the bump. (*b*) Shear stress at the interface between the two fluids along the channel. (*c*) Horizontal velocity u_h at the interface $y = h(x)$ along the channel. (*d*) Horizontal velocity u_0 in the middle of the channel at $y = 0$ along the channel. All quantities are dimensionless.

(figure 21*a*) do change due to the shear-thinning rheology of fluid *A*. Quantitatively, the interfacial shear stress is increased by only 1.4 times under the bump as compared with far from the bump in our calculations here.

We now compare the situations where we have a solution of $10\,\mathrm{mg\,ml^{-1}}$ BSA and a solution of $10\,\mathrm{mg\,ml^{-1}}$ Hb mixed in bumpy channels. As table 4 shows, the viscosity ratios Λ are similar (0.20 versus 0.22) and the concentrations are identical (we can assume a similar crowding agent effect on the mixing then). Experimentally, mixing occurs after 3 half-cycles for Hb and 7 half-cycles for BSA. Our model shows that the dimensionless striation thickness is 0.0017 for Hb and 0.0036 for BSA after 3 bumps in the bumpy serpentine mixer: the dimensionless striation thickness is much thinner for Hb than for BSA after 3 bumps in the bumpy mixer. The model confirms then the qualitative trend of the experiment. In the meantime, the model would predict better mixing for a '*shear-thickening*' fluid: it shows the dimensionless striation thickness to be 0.00107 after 3 bumps in the bumpy serpentine mixer for a shear-thickening fluid with $n = 1.5$ and $\Lambda = 0.20$, all other parameters being equal.

B.2. *Slip difference*

We turn now to the slip difference between bumps and no bumps in the case of a non-Newtonian fluid (figure 22). We observe that, for sufficiently long times, after the plug has gone past the bump, there is a persistent non-zero slip difference. This plateau is negative for a shear-thickening fluid ($n > 1$), positive for a shear-thinning fluid ($n < 1$), equal to zero for a Newtonian fluid (see figure 11*a*).
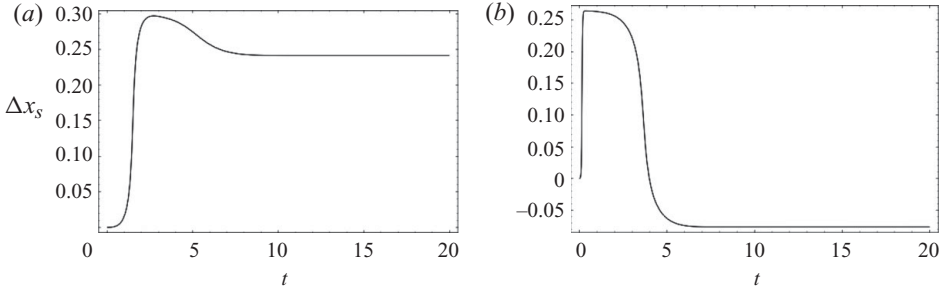
FIGURE 22. Slip difference $\Delta x_s(t) = x_{s_b}(t) - x_{s_{nb}}(t)$ for (a) a shear-thinning fluid where $n = 0.1$, (b) for a shear-thickening fluid where $n = 1.5$. All quantities are dimensionless.

The amplitude of the persistent slip difference can be determined analytically. From previous work, we can write:

$$\frac{\mathrm{d}x_0}{\mathrm{d}t} = u_0(x_0), \tag{B 6}$$

$$\frac{\mathrm{d}x_h}{\mathrm{d}t} = u_h(x_h), \tag{B 7}$$

where

$$u_0(x_0) = \left(-\frac{\mathrm{d}p}{\mathrm{d}x}\right)^{1/n} / ((1/n + 1)\Lambda)[h^{1/n+1}(x_0)] + \frac{1}{2}\frac{\mathrm{d}p}{\mathrm{d}x}\left[h^2(x_0) - d_w^2(x_0)\right], \tag{B 8}$$

$$u_h(x_h) = \frac{1}{2}\frac{\mathrm{d}p}{\mathrm{d}x}\left[h^2(x_h) - d_w^2(x_h)\right]. \tag{B 9}$$

Note that $u_0(x_0) \sim u_0(\infty)$ and $u_h(x_h) \sim u_h(\infty)$ as $x_0 \geqslant 1$, $x_h \geqslant 1$. Therefore, from (B.6) through (B.9), we obtain, for $x_0 \geqslant 1$, $x_h \geqslant 1$: for large t,

$$x_0(t) = 1 + u_0(\infty)t - \int_0^1 \frac{u_0(\infty)}{u_0(x)}\,\mathrm{d}x, \tag{B 10}$$

$$x_h(t) = 1 + u_h(\infty)t - \int_0^1 \frac{u_h(\infty)}{u_h(x)}\,\mathrm{d}x. \tag{B 11}$$

Therefore, we derive

$$x_{s_{nb}}(t) = (u_0(\infty) - u_h(\infty))t, \tag{B 12}$$

$$x_{s_b}(t) = (u_0(\infty) - u_h(\infty))t + \int_0^1 \left(\frac{u_h(\infty)}{u_h(x)} - \frac{u_0(\infty)}{u_0(x)}\right)\mathrm{d}x, \tag{B 13}$$

and eventually

$$\Delta x_s(t) = \int_0^1 \left(\frac{u_h(\infty)}{u_h(x)} - \frac{u_0(\infty)}{u_0(x)}\right)\mathrm{d}x. \tag{B 14}$$

By defining

$$D(x) = \frac{u_h(\infty)}{u_h(x)} - \frac{u_0(\infty)}{u_0(x)}, \tag{B 15}$$

we then find that $\Delta x_s(t)$ depends on the sign of $D(x)$. In other words, the persistent slip difference can be maximized in maximizing the value of
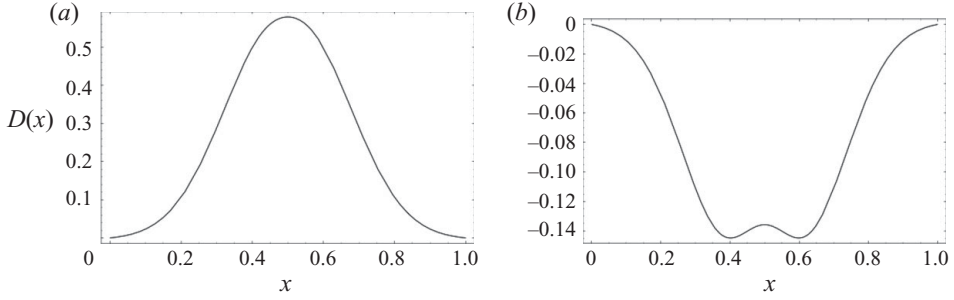
$$\int_0^1 D(x)\,\mathrm{d}x.$$

FIGURE 23. $D(x) = u_h(\infty)/u_h(x) - u_0(\infty)/u_0(x)$ for (a) a shear-thinning fluid where $n = 0.1$, (b) a shear-thickening fluid where $n = 1.5$. All quantities are dimensionless.

For a non-Newtonian fluid, we found that, for large t,

$$\Delta x_s = x_{s_b} - x_{s_{nb}} = \int_0^1 \frac{G(x)}{u_0(x)u_h(x)} \, dx, \qquad (B\,16)$$

where $G(x) = u_h(\infty)u_0(x) - u_h(x)u_0(\infty)$. Literally,

$$G(x) = \frac{1}{2\Lambda(1/n+1)} \left[\left(-\frac{dp}{dx}\right)^{1/n} \left(-\frac{dp}{dx}\right)_\infty h^{1/n+1} \{d_{w_\infty}^2 - h_\infty^2\} \right.$$
$$\left. - \left(-\frac{dp}{dx}\right)_\infty^{1/n+1} h_\infty^{1/n+1} \left(-\frac{dp}{dx}\right) \{d_w^2(x) - h^2(x)\} \right]. \quad (B\,17)$$

Now consider the particular case where $n = 1$ corresponding to a Newtonian fluid:

$$G(x) = \frac{1}{4\Lambda} \left(-\frac{dp}{dx}\right) \left(-\frac{dp}{dx}\right)_\infty \{h_\infty^2 d_w^2 - h^2 d_{w_\infty}^2\}. \qquad (B\,18)$$

Recall that for a Newtonian fluid, we find the following analytical solution for the interface $h(x) = h_\infty^2 d_w^2/d_{w_\infty}^2$, which directly leads to $G(x) = 0$ and so $\Delta x_s = 0$. When now $n \neq 1$, we look at the variations of (B.17). We assume as in the numerical inputs used so far that $(-dp/dx)_\infty = 1$, which leads to

$$G(x) = \frac{1}{2\Lambda(1/n+1)} \left[\left(-\frac{dp}{dx}\right)^{1/n} h^{1/n+1} \{d_{w_\infty}^2 - h_\infty^2\} \right.$$
$$\left. - \left(-\frac{dp}{dx}\right) h_\infty^{1/n+1} \{d_w^2 - h^2\} \right]. \qquad (B\,19)$$

$G(x) > 0$ if and only if $f(x, n) > 0$, where

$$f(x, n) = \left(-\frac{dp}{dx}\right)^{1/n} (h/h_\infty)^{1/n} - \frac{(d_w^2 - h^2)}{(d_{w_\infty}^2 - h_\infty^2)} \left(-\frac{dp}{dx}\right) \frac{h_\infty}{h}.$$

We look at the variations of f with respect to n:

$$\frac{\partial f}{\partial n} = -\frac{1}{n^2} \ln [(-dp/dx)(h/h_\infty)] \, e^{(1/n)\ln[(-dp/dx)((h/h_\infty))]}. \qquad (B\,20)$$

Note that $(-dp/dx)(h/h_\infty) > 1$ as $\tau_{AB} > \tau_{AB}(\infty)$ for any x. In this way, $\partial f/\partial n < 0$. As we showed $f(x, 1) = 0$, we necessarily have $f(x, n) < 0$ for $n > 1$ and $f(x, n) > 0$ for $n < 1$. If we come back to (B.17), we see that the particle P_h accelerates less than

the particle P_0 under the bump for a shear-thinning fluid whereas the particle P_h accelerates more than the particle P_0 under the bump for a shear-thickening fluid (see figure 23). For a Newtonian fluid, the particle P_h accelerates as much as the particle P_0 under the bump.

REFERENCES

ANDREAS, J. M., HAUSER, E. A. & TUCKER, W. B. 1938 Boundary tension by pendant drops. *J. Phys. Chem.* **42**, 1001–1019.

AREF, H. 1984 Stirring by chaotic advection. *J. Fluid. Mech.* **143**, 1–21.

AREF, H. 2002 The development of chaotic advection. *Phys. Fluids* **14**, 1315–1325.

BEHRENS, R. A., CROCHET, M. J., DENSON, C. D. & METZNER, A. B. 1987 Transient free-surface flows: motion of a fluid advancing in a tube. *AIChE J.* **33**, 1178–1186.

BIRD, R. B., ARMSTRONG, R. C. & HASSAGER, O. 1987 *Dynamics of Polymeric Liquids*. Wiley.

BRETHERTON, F. P. 1961 The motion of long bubbles in tubes. *J. Fluid Mech.* **10**, 166–188.

BRINGER, M. R., GERDTS, J. C., SONG, H., TICE, J. D. & ISMAGILOV, R. F. 2004 Microfluidic systems for chemical kinetics that rely on chaotic mixing in droplets. *Phil. Trans. R. Soc. Lond*. A **362**, 1087–1104.

CHANG, C. H. & FRANSES, E. I. 1995 Adsorption dynamics of surfactants at the air/water interface - a critical review of mathematical models, data, and mechanisms. *Colloids Surf.* A*: Physichochem. Engng Asp.* **100**, 1–45.

COYLE, D. J., BLAKE, J. W. & MACOSKO, C. W. 1987 The kinematics of fountain flow in mold-filling. *AIChE J.* **33**, 1168–1177.

D'ALESSANDRO, D., DAHLEH, M. & MEZIC, I. 1999 Control of mixing in fluid flow: a maximum entropy approach. *IEEE Trans. Autom. Control* **44**, 1852–1863.

DEEN, W. 1998 *Analysis of Transport Phenomena*. Oxford University Press.

DUFFY, D. C., MCDONALD, J. C., SCHUELLER, O. J. A. & WHITESIDES, G. M. 1998 Rapid prototyping of microfluidic systems in poly(dimethylsiloxane). *Anal. Chem.* **70**, 4974–4984.

EDWARDS, D., BRENNER, H. & WASAN, D. 1991 *Interfacial Transport Processes and Rheology*. Butterworth–Heinemann.

EGGLETON, C. D., PAWAR, Y. P. & STEBE, K. J. 1999 Insoluble surfactants on a drop in an extensional flow: a generalization of the stagnated surface limit to deforming interfaces. *J. Fluid Mech.* **385**, 79–99.

ELLIS, R. J. 2001 Macromolecular crowding: obvious but underappreciated. *Trends Biochem. Sci.* **26**, 597–604.

GRAHAM, D. E. & PHILLIPS, M. C. 1979*a* Proteins at liquid interfaces 1. Kinetics of adsorption and surface denaturation. *J. Colloid Interface Sci.* **70**, 403–414.

GRAHAM, D. E. & PHILLIPS, M. C. 1979*b* Proteins at liquid interfaces 2. Adsorption-isotherms. *J. Colloid Interface Sci.* **70**, 415–426.

HALL, D. & MINTON, A. P. 2003 Macromolecular crowding: qualitative and semi quantitative successes, quantitative challenges. *Biochem. Biophys. Acta* **1649**, 127–139.

HODGES, S. R., JENSEN, O. E. & RALLISON, J. M. 2004 The motion of a viscous drop through a cylindrical tube. *J. Fluid Mech.* **501**, 279–301.

IKEDA, S. & NISHINARI, K. 2000 Intermolecular forces in bovine serum albumin solutions exhibiting solidlike mechanical behaviours. *Biomacromolecules* **1**, 757–763.

JACOB, A. M. & GAVER, D. P. 2005 An investigation of the influence of cell topography on epithelial mechanical stresses during pulmonary airway reopening. *Phys. Fluids* **17**, 031052-1–031052-11.

JENSEN, O. E., CHINI, G. P. & KING, J. R. 2004 Thin-film flows near isolated bumps and interior corners. *J. Engng Math.* **50**, 289–309.

JENSEN, O. E. & GROTBERG, J. B. 1999 The spreading of heat or soluble surfactant along a thin liquid film. *Phys. Fluids* A**5**, 58–68.

LIAU, A., KARNIK, R., MAJUMDAR, A. & CATE, J. H. D. 2005 Mixing crowded biological solutions in milliseconds. *Anal. Chem.* **77**, 7618–7625.

Liu, R. H., Stremler, M. A., Sharp, K. V., Olsen, M. G., Santiago, J. G., Adrian, R. J., Aref, H. & Beebe, D. J. A. 2000 Passive mixing in a three-dimensional serpentine channel. *J. Microelectromech. Syst.* **9**, 190–197.

Minton, A. P. 2001 The influence of macromolecular crowding and macromolecular confinement on biochemical reactions in physiological media. *J. Biol. Chem.* **276**, 10577–10580.

Monkos, K. 1994 Viscometric study of human, bovine, equine and ovine hemoglobin in aqueous solution. *Intl J. Biol. Macromol.* **16**, 31–35.

Monkos, K. 1996 Viscosity of bovine serum albumin aqueous solutions as a function of temperature and concentration. *Intl J. Biol. Macromol.* **18**, 61–68.

Muradoglu, M. & Stone, H. A. 2005 Mixing in a droplet moving through a serpentine channel: a computational study. *Phys. Fluids* **18**, 073305-1–073305-9.

Muradoglu, M. & Stone, H. A. 2007 Motion of large bubbles in curved channels. *J. Fluid Mech.* **570**, 455–466.

Ottino, J. M. 1989 The kinematics of mixing: stretching, chaos and transport. Cambridge University Press.

Ottino, J. M. & Wiggins, S. 2004 Introduction: Mixing in microfluidics. *Phil. Trans. R. Soc. Lond.* A **362**, 923–935.

Park, C-W. 1992 Influence of soluble surfactants on the motion of a finite bubble in a capillary tube. *Phys. Fluids* **A4**, 2335–2347.

Roy, R. V., Roberts, A. J. & Simpson, M. E. 2002 A lubrication model of coating flows over a curved substrate in space. *J. Fluid Mech.* **454**, 235–261.

Satyanarayana, S., Karnik, R. & Majumdar, A. 2005 Stam-and-stick room-temperature bonding technique for microdevices. *J. Microelectromech. Syst.* **14**, 392–399.

Song, H. & Ismagilov, R. F. 2003 Millisecond kinetics on a microfluidic chip using nanoliters of reagents. *J. Am. Chem. Soc.* **125**, 14613–14619.

Song, H., Tice, J. D. & Ismagilov, R. F. 2003 A microfluidic system for controlling reaction networks in time. *Angew. Chem. Intl Ed.* **42**, 768–772.

Stauffer, C. E. 1965 Measurement of surface tension by pendant drop technique. *J. Phys. Chem.* **69**, 1933–1938.

Stroock, A. D., Dertinger, S. K. W., Ajdari, A., Mezic, I., Stone, H. A. & Whitesides, G. M. 2002 Chaotic mixer for microchannels. *Science* **295**, 647–651.

Sturman, R., Ottino, J. M. & Wiggins, S. 2006 *The Mathematical Foundations of Mixing: The Linked Twist Map as a Paradigm in Applications: Micro to Macro, Fluids to Solids.* Cambridge University Press.

Wiggins, S. & Ottino, J. M. 2004 Foundations of chaotic mixing. *Phil. Trans. R. Soc. Lond.* A **362**, 937–970.

Wolfram Research, Inc. 2005 *Mathematica Edition: Version 5.2.* Wolfram Research, Inc.